Rethinking simultaneous suppression in visual cortex via compressive spatiotemporal population receptive fields

Authors

Eline R Kupers[1*], Insub Kim[1], Kalanit Grill-Spector[1,2]

Affiliations

[1] Department of Psychology, Stanford University, CA, USA
[2] Wu Tsai Neurosciences Institute, Stanford University, CA, USA
* Corresponding author. Email to: ekupers@stanford.edu

Acknowledgements
We thank Brian Wandell for fruitful discussions. This research was supported by the US NIH NEI R01 EY023915 (KGS). Funders had no role in study design, data collection and analysis, or decision to submit the manuscript.

Author contributions
E.R.K and K.G.S. designed the experiment. K.G.S. provided funding. E.R.K. and I.K. collected data and wrote computational framework. E.R.K. analyzed the data. K.G.S. oversaw computational framework and data analysis. E.R.K and K.G.S. wrote the manuscript. I.K. provided feedback on manuscript.

1 Abstract

When multiple visual stimuli are presented simultaneously in the receptive field, the neural response is suppressed compared to presenting the same stimuli sequentially. The prevailing hypothesis suggests that this suppression is due to competition among multiple stimuli for limited resources within receptive fields, governed by task demands. However, it is unknown how stimulus-driven computations may give rise to simultaneous suppression. Using fMRI, we find simultaneous suppression in single voxels, which varies with both stimulus size and timing, and progressively increases up the visual hierarchy. Using population receptive field (pRF) models, we find that compressive spatiotemporal summation rather than compressive spatial summation predicts simultaneous suppression, and that increased simultaneous suppression is linked to larger pRF sizes and stronger compressive nonlinearities. These results necessitate a rethinking of simultaneous suppression as the outcome of stimulus-driven compressive spatiotemporal computations within pRFs, and open new opportunities to study visual processing capacity across space and time.

2 Introduction

The human visual system has limited processing capacity. We are worse at processing multiple stimuli presented at once than when the identical stimuli are shown one after the other in the same location. This drop in performance has been observed in a variety of visual tasks, such as searching for a target among distractors[1,2], recognizing an object when surrounded by flankers[3], or keeping multiple items in short-term visual working memory[4].

A prevailing explanation based on the influential biased-competition theory[5-7], is that visual processing capacity is determined by the computational resources afforded by receptive fields, where the visual system prioritizes inputs that are behaviorally relevant for further processing. When a visual stimulus is presented alone in the receptive field, the item can be fully processed with the limited neural resources. However, when multiple stimuli are presented in the receptive field these stimuli compete for neural resources, resulting in a reduced neurophysiological response. Indeed, when multiple stimuli are presented simultaneously within a neuron's receptive field, the response is lower than when the identical stimuli are presented one after the other in sequence[7-9]—a phenomenon called simultaneous suppression.

Simultaneous suppression is robust and prevalent. It has been observed from the level of single-neuron spiking[7-9], all the way to the level of entire visual areas using fMRI[6,10-13], and the effect is large: up to 2-fold amplitude differences between sequential and simultaneous presentations of otherwise identical stimuli[6,10,13]. Stemming from the idea that competition for neural resources can be resolved by task or behavioral demands[5], a large body of research has examined how visual attention[6,7,14,15] and context[11,12] modulate simultaneous suppression. However, it is unknown how simple stimulus-driven computations within receptive fields may give rise to simultaneous suppression in the first place. Thus, the goal of the present study is to operationalize and elucidate the computational mechanisms underlying simultaneous suppression in human visual cortex.

One hypothesis stemming from the biased-competition theory is that simultaneous suppression will only occur in neurons which receptive fields are large enough to encompass several stimuli[10]. It is well documented that the size of receptive fields[16] and population receptive fields (pRFs, aggregate receptive field of the neuronal population in an fMRI voxel[17,18]) progressively increase from lower to higher areas up the visual hierarchy. Consistent with this hypothesis, several studies reported that simultaneous suppression systematically increases across the visual hierarchy and is absent in V1[7,10,13], suggesting that the lack of suppression in V1 is because its receptive fields are too small to encompass multiple visual stimuli[7,10,13].

Next to increasing receptive field sizes, compressive nonlinearities also progressively increase up the visual hierarchy. V1 pRFs sum visual inputs mostly linearly: spatially across the visual field and temporally over the duration of the stimulus[19,20]. Thus, regardless of size, V1 pRFs predict identical responses to simultaneous and sequential presentations for which the stimuli are identical in location and duration, and only differ in sequence order. However, pRFs in subsequent visual areas perform subadditive summation of the visual input, both spatially[20-23] and temporally[24-36]. Consequently, responses to bigger or longer visual stimuli are typically smaller than the sum of responses to smaller or shorter stimuli. Therefore, we hypothesize that sub-additive (or compressive) summation within receptive fields may give rise to simultaneous suppression.

We consider two possible compressive neural mechanisms that may generate simultaneous suppression. One possibility is compressive spatial summation of visual inputs within receptive fields. This mechanism predicts that the response to multiple stimuli presented together within the pRF (as in simultaneous condition) will be lower than the sum of responses to the individual stimuli shown alone (as in sequential condition). As the duration of stimuli are matched between the simultaneous and sequential conditions, the spatial hypothesis predicts that the level of simultaneous suppression will only depend on the spatial overlap between the stimuli and the pRF.

A second possibility is compressive spatiotemporal summation. Neuronal responses to visual stimuli typically show an initial strong transient response (lasting for 100-200 ms) followed by a weaker sustained response lasting for the duration of the stimulus[25,36-40], and a transient response at stimulus offset[34,36,39]. These nonlinear temporal dynamics suggest that presenting all stimuli at once in the pRF (as in the simultaneous condition) results in two transients (at stimulus onset and offset). This response will be lower than the accumulated response induced by multiple transients in the pRF when presenting the stimuli one-by-one in rapid fashion (as in the sequential condition). Thus, the spatiotemporal hypothesis predicts that the level of simultaneous suppression will depend on both the spatial overlap between the stimuli and the pRF and the number of visual transients in the pRF.

Here, we used fMRI and a computational pRF framework to distinguish between these hypotheses. We conducted two fMRI experiments. In the first (SEQ-SIM, **Fig 1A**), we measured responses to sequentially or simultaneously presented stimuli and examined how stimulus size and presentation timing affect the level of simultaneous suppression in each voxel (**Fig 1B**). In the second experiment (retinotopy, **Fig 1C**), we estimated each voxel's spatial pRF parameters and used those parameters in a pRF modeling framework to predict the BOLD time series for each voxel in the SEQ-SIM experiment. We implemented several pRF models in our modeling framework to computationally test the spatial and spatiotemporal hypotheses. To test the spatial hypothesis, we used a

compressive spatial summation (CSS) pRF model[22] as it successfully predicts subadditive responses to stimuli of different apertures in pRFs across the visual hierarchy. To test the spatiotemporal hypothesis, we used a novel compressive spatiotemporal (CST) summation pRF model[41], which predicts fMRI responses in each voxel to rapid and brief stimuli in units of visual degrees and milliseconds, and captures spatiotemporal subadditivity for large range of spatial and temporal stimulus conditions.

3 Results

To investigate what factors affect simultaneous suppression, we designed an fMRI experiment in which participants viewed colorful patterned square stimuli in upper and lower quadrants while performing a 1-back RSVP fixation task. Squares could either be presented sequentially (one after the other, in random order) or simultaneously (all at once) (**Fig 1A**). For each pair of sequential and simultaneous conditions, individual square presentation is identical in size and duration within an 8-s block such that linear summation of visual inputs in space and time will generate identical responses for both sequence types. To distinguish between spatial and spatiotemporal mechanisms of simultaneous suppression, we varied square size and timing (**Fig 1B**). Additionally, participants completed an independent retinotopy experiment[42] to delineate visual areas and estimate spatial pRF parameters in each voxel (**Fig 1C**).

In each visual area, we measured BOLD responses in voxels which pRF centers overlapped the quadrants with SEQ-SIM stimuli. We then determined how spatial and temporal stimulus properties affect simultaneous suppression for each pRF across visual areas spanning ventral, lateral, and dorsal processing streams. We predict that if simultaneous suppression is of spatial origin, there will be greater suppression in higher-level than early visual areas because those higher-level areas contain larger pRFs that will overlap multiple squares and also show greater spatial compression[22]. Additionally, we predict that varying square size but not timing will affect simultaneous suppression. If simultaneous suppression is of spatiotemporal origin, in addition to observing greater suppression for larger pRFs in higher-level areas, we also predict stronger suppression for long (1 s) than short (0.2 s) presentations because the former has longer sustained stimulus periods, resulting in four times fewer visual transients in the 8-s blocks than the latter (**Fig 1B**).

To give a gist of the data, we first show results from example voxels in early (V1) and higher-level (VO1/2) areas of the ventral stream. These visual areas differ in overall pRF size (and spatial compression): V1 pRFs are small and typically overlap only one square, and VO1/2 pRFs are large and overlap multiple squares.

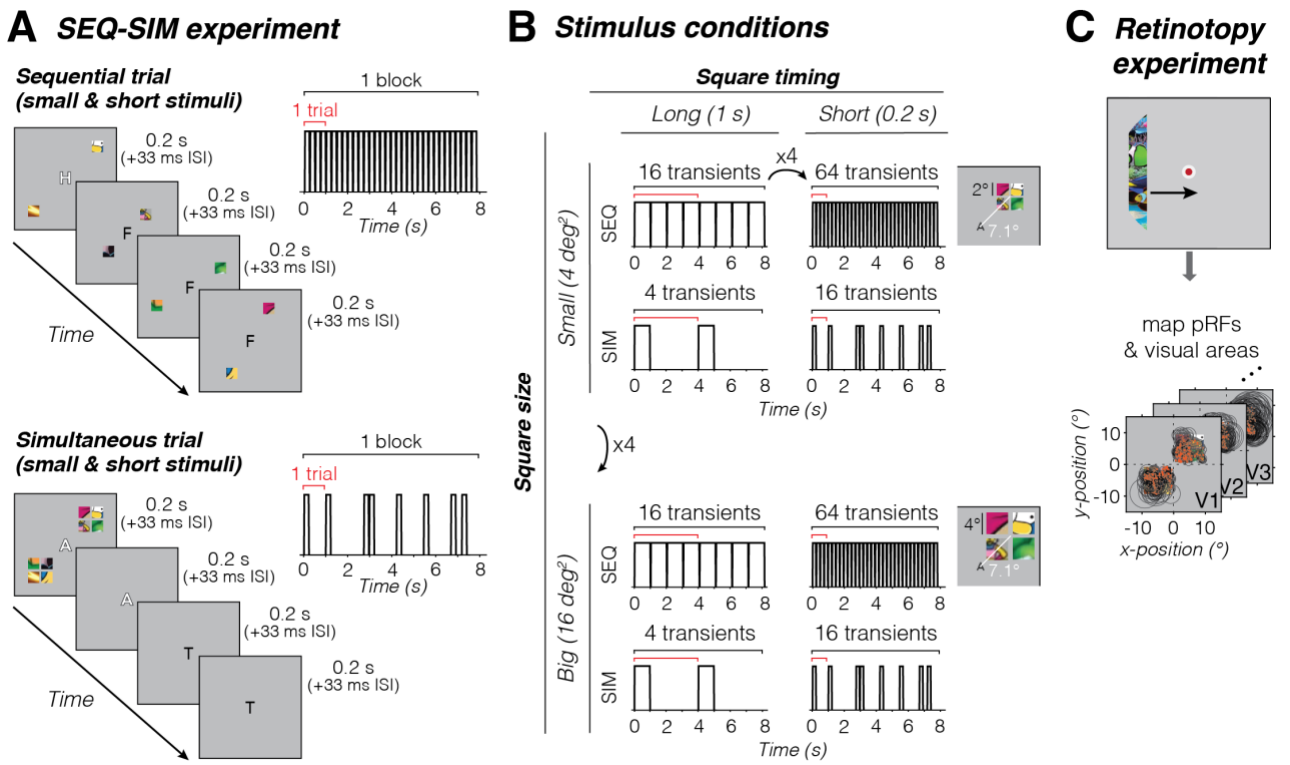

Figure 1. Overview of fMRI experiments. (A) SEQ-SIM experiment. Example trial sequences for small and short stimuli. Four colorful squares were presented in the upper left and lower right quadrants, presented either sequentially in random order (top) or simultaneously (bottom) interspersed by blank periods to match the trial duration. Thus for each SEQ-SIM pairing, individual squares were shown for the same duration within a single trial (red bracket). Trials were repeated within an 8-s block (black bracket), where square content was updated for each trial. *Insets:* Example time course of an 8-s block for sequential (top) and simultaneous (bottom) stimuli. Observers performed a 1-back RSVP letter task at fixation. Letter is enlarged for visibility. **(B) Stimulus conditions.** Square stimuli were shown in one of two sizes (4 or 16 deg^2) and in one of two presentation timings (0.2 s or 1 s). Number of trials per block was adjusted to create a 4:1 ratio in number of transients (stimulus onsets or offsets) for short vs long durations. The number of transients indicated is based on a pRF overlapping all four squares, e.g., for 1-s sequentially-presented squares there are 16 transients per block: 4 stimulus frames x 2 on/offsets x 2 trials. If a pRF overlaps only a single square (time course not shown), the number of transients will be identical for SEQ and SIM pairs. **(C) Retinotopy experiment.** Observers viewed bars containing cropped cartoon stimuli traversing the visual field (top) while fixating and performing a color change detection task at fixation[42]. Data were used to define visual areas and select pRFs with centers overlapping stimulus quadrants in the main experiment (bottom). Fixation dot is enlarged for visibility.

3.1 V1 voxels with small pRFs show modest to no simultaneous suppression

As predicted, for a single V1 voxel with a small pRF overlapping only a single square, we find similar responses for simultaneous vs sequential presentations in the two stimulus sizes and presentation timings (**Fig 2A**). In other words, this voxel shows no simultaneous suppression. Additionally, we observe that for this V1 voxel responses are larger for short presentations (with many visual transients) vs long presentations (few visual transients). However, there is no difference in the response amplitude for small vs big squares of the same duration (left vs right panels).

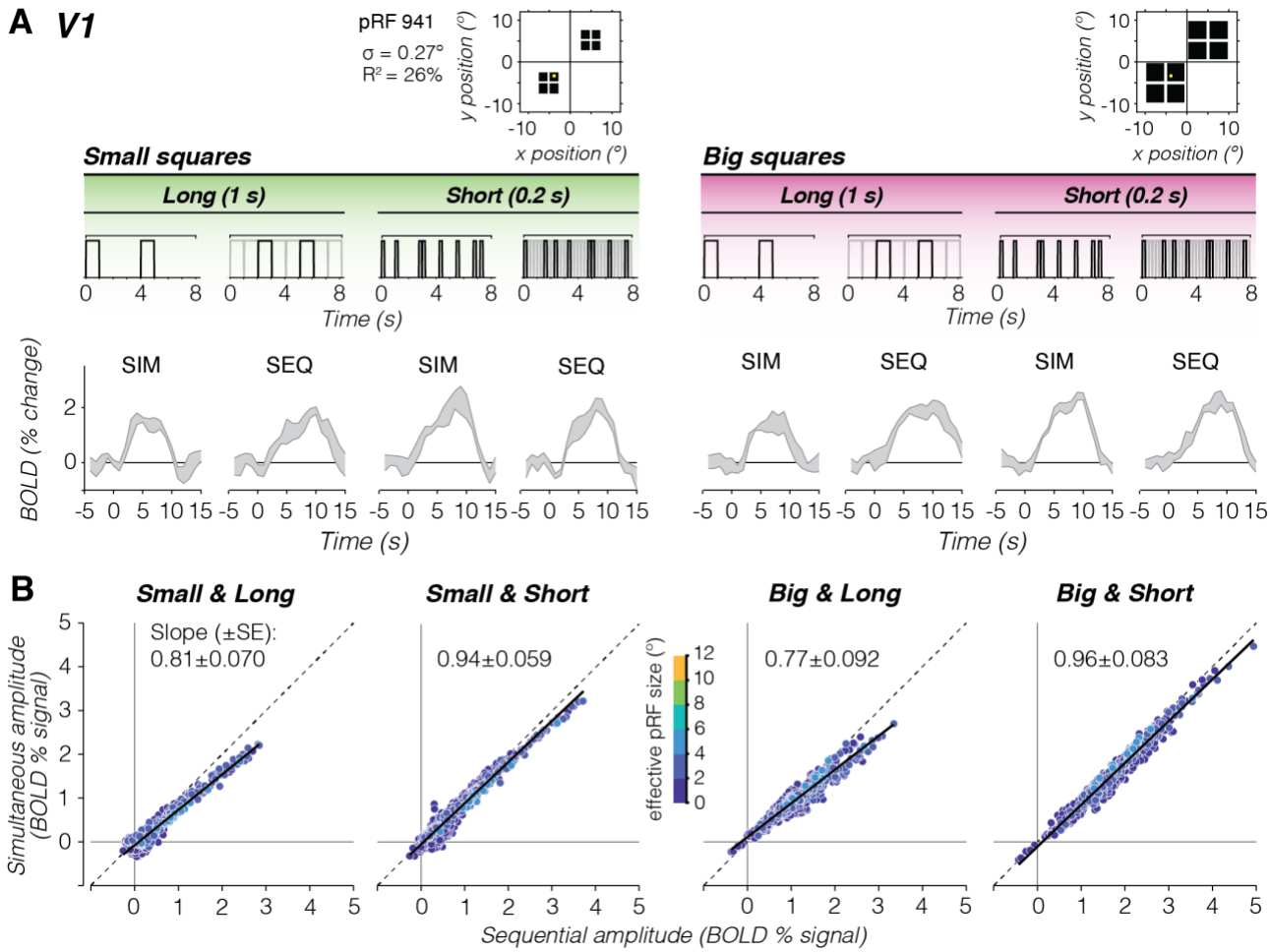

Figure 2. V1 voxels show no to little simultaneous suppression. (A) Example V1 voxel with small pRF overlapping a single square. The example voxel's pRF (yellow circle) is superimposed on square locations (black). Gray time courses show the example voxel's average BOLD time series ± SEM across block repeats for each stimulus condition. Above each time series is an example stimulus sequence for each condition in an 8-s block. *Gray sequence:* time course including all square stimuli. *Black sequence:* time course for small pRF overlapping one square. **(B) Relation between BOLD amplitude (% signal) for simultaneous vs sequential blocks, for each size/duration condition.** Data include all V1 voxels from participant S3 with pRFs overlapping squares, averaged across a 9-s time window centered on the peak response. Each dot is a voxel, colored by effective pRF size from the retinotopy modelfit ($\sigma/\sqrt{n}$). *Dashed line:* No suppression. *Solid black line:* Linear mixed model (LMM) line fit for this participant's V1 data. Slope (±SE) are from this participant's line fit.

To assess simultaneous suppression, we compare single voxel response amplitudes for simultaneous vs sequential presentations for a given stimulus condition. No suppression will result on voxels falling on the identity line, whereas simultaneous suppression will result in voxels below the diagonal. In V1, we find that many voxels fall closely or just below the identity line (**Fig 2B**, example participant; **Supplementary Fig 1,** all participants) even as response levels were higher for short vs long stimulus presentation timings. To quantify this relationship, we fit a linear mixed model (LMM) relating the simultaneous amplitude to the sequential amplitude across V1 voxels using a

fixed interaction effect for conditions, and random participant effect (intercepts and slopes vary per participant and condition, **Equation 1**). LMM slopes of 1 indicate no suppression, slopes less than 1 indicate simultaneous suppression, where smaller slopes correspond to stronger suppression levels.

Across participants, the LMM captures 86% of the variance in V1, with the following average (± SEM) suppression levels: small and long squares: 0.81±0.069 ($CI_{95\%}$=0.56–1.06), small and short squares: 0.85±0.058 ($CI_{95\%}$=0.73–0.96), big and long squares: 0.85±0.090 ($CI_{95\%}$=0.56–1.4), and big and short squares: 0.84±0.081 ($CI_{95\%}$=0.57–1.1). Thus, V1 voxels with relatively small pRFs show modest to no simultaneous suppression.

3.2 Strong simultaneous suppression for large pRFs in higher-level visual areas

For a single VO voxel with a large pRF overlapping all four large squares, we find lower responses for simultaneous than sequential presentations for both square sizes and presentation timings (**Fig 3A**). In other words, this voxel shows simultaneous suppression across all experimental conditions. Additionally, we observe that the overall response amplitudes of this voxel are larger for the big squares and short presentations compared to the small squares and long presentations.

We observe this pattern of results across VO voxels. Plotting the average amplitude for simultaneous vs sequential presentations, we find a linear relationship between responses to simultaneous and sequential pairings, where voxels show simultaneous suppression and the level of suppression varies across experimental conditions (**Fig 3B**, example participant; **Supplementary Fig 1,** all participants). This relationship is not a given, as simultaneous suppression could have tapered off with response level. Instead, our data suggests that suppression can be summarized with a single slope per visual area and experimental condition.

Quantitative analyses using a LMM (R^2=97%) revealed significant simultaneous suppression varying with stimulus size and duration, with the following suppression levels: small and long squares: 0.40±0.075 ($CI_{95\%}$=0.15–0.65), small and short squares: 0.65±0.052 ($CI_{95\%}$=0.55–0.75), big and long squares: 0.62±0.11 ($CI_{95\%}$=0.31–0.93), and big and short squares: 0.70±0.033 ($CI_{95\%}$=0.54–0.87). Notably, for stimuli of the same duration, there is larger suppression (smaller slopes) for the small vs big squares. However, for the same square size, there is larger suppression for long vs short presentation timings. This suggests that in VO1/2, in addition to stimulus' spatial overlap with the pRF, timing also contributes to simultaneous suppression.

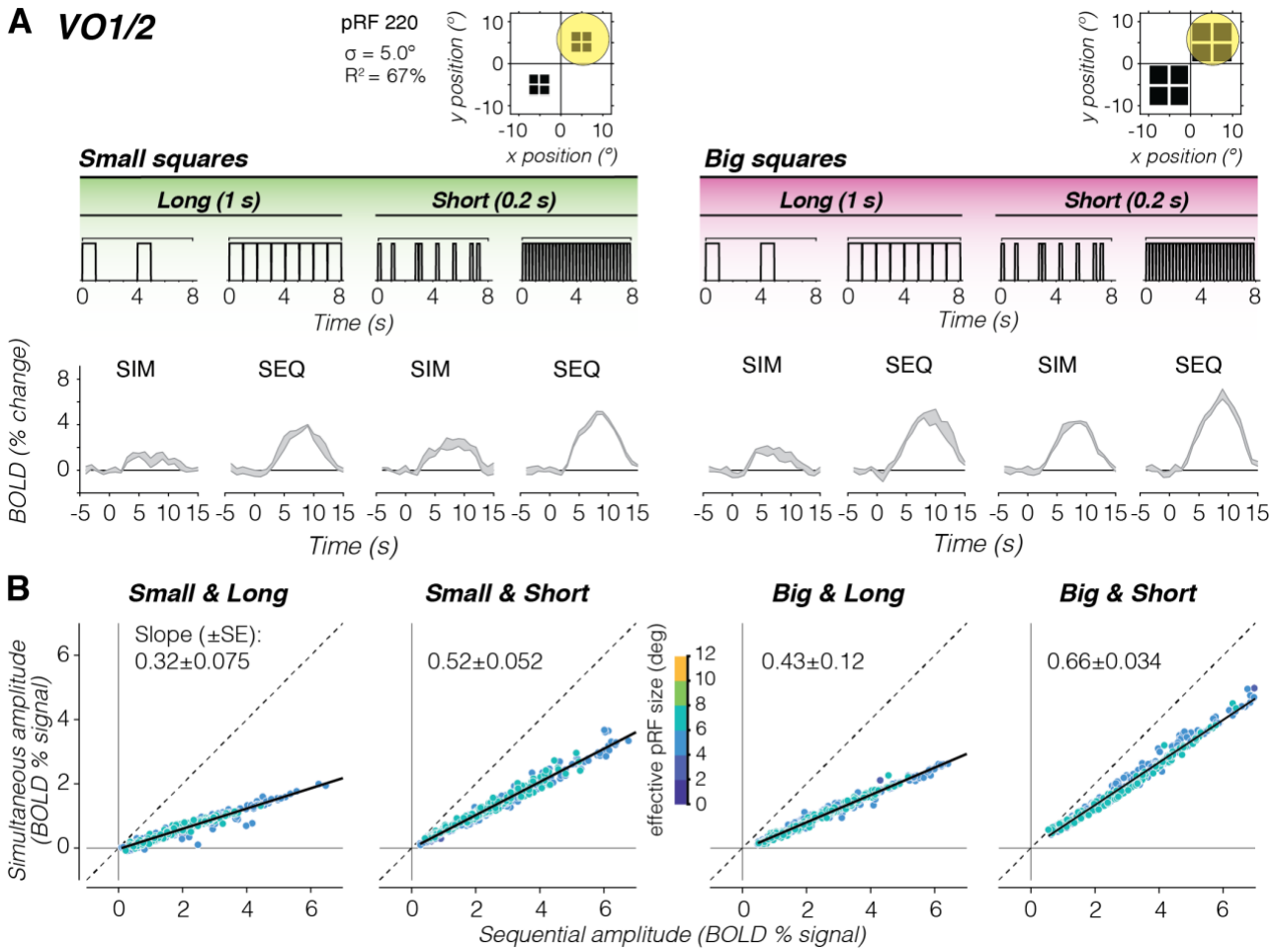

Figure 3. Individual VO1/2 voxels with large pRFs show strong simultaneous suppression effects. Same layout as Fig 2, but for high-level visual area VO1/2. Data are from participant S3. (A) Example time series of a VO1 voxel. Voxel has a large pRF that covers all the four squares of both sizes (yellow circle). **(B) Simultaneous vs. sequential BOLD amplitude for all voxels in VO1/2.** *Dashed line:* No suppression; *Solid black line:* LMM line fit for this participant VO1/2 data.

3.3 Simultaneous suppression increases up the visual hierarchy and depends on stimulus size and presentation timing

We next quantified the relationship between responses in simultaneous vs sequential presentations across the visual hierarchy. Our data show four findings. First, in each visual area and stimulus condition, we find a linear relationship between voxels' responses to simultaneous and sequential stimuli (**Fig 4A**, big and short stimuli; **Supplementary Fig 1**, all conditions). Second, when quantifying this linear relationship by its slope, we find that simultaneous suppression is prevalent at the voxel level in almost every visual area across participants. Third, across all stimulus conditions, we find that suppression levels progressively increase from early visual areas (V1 to V2 to V3) to intermediate areas (hV4, LO1/2, V3A/B), with the strongest simultaneous suppression in TO1/2 (**Fig 4B** and **Supplementary Table 1**). Fourth, up the visual hierarchy, simultaneous suppression levels

depend on stimulus condition. In particular, higher-level visual areas show stronger suppression for long vs short presentation timings, and stronger suppression for small vs big square sizes. A two-way repeated measures ANOVA revealed significant effects of visual area ($F(8)=23$, $p=7.3\times10^{-27}$) and stimulus condition ($F(3)=27$, $p=2.3\times10^{-15}$) on suppression slopes. There was no significant interaction between stimulus condition and visual area (**Supplementary Table 2;** post-hoc Bonferroni-corrected t-tests).

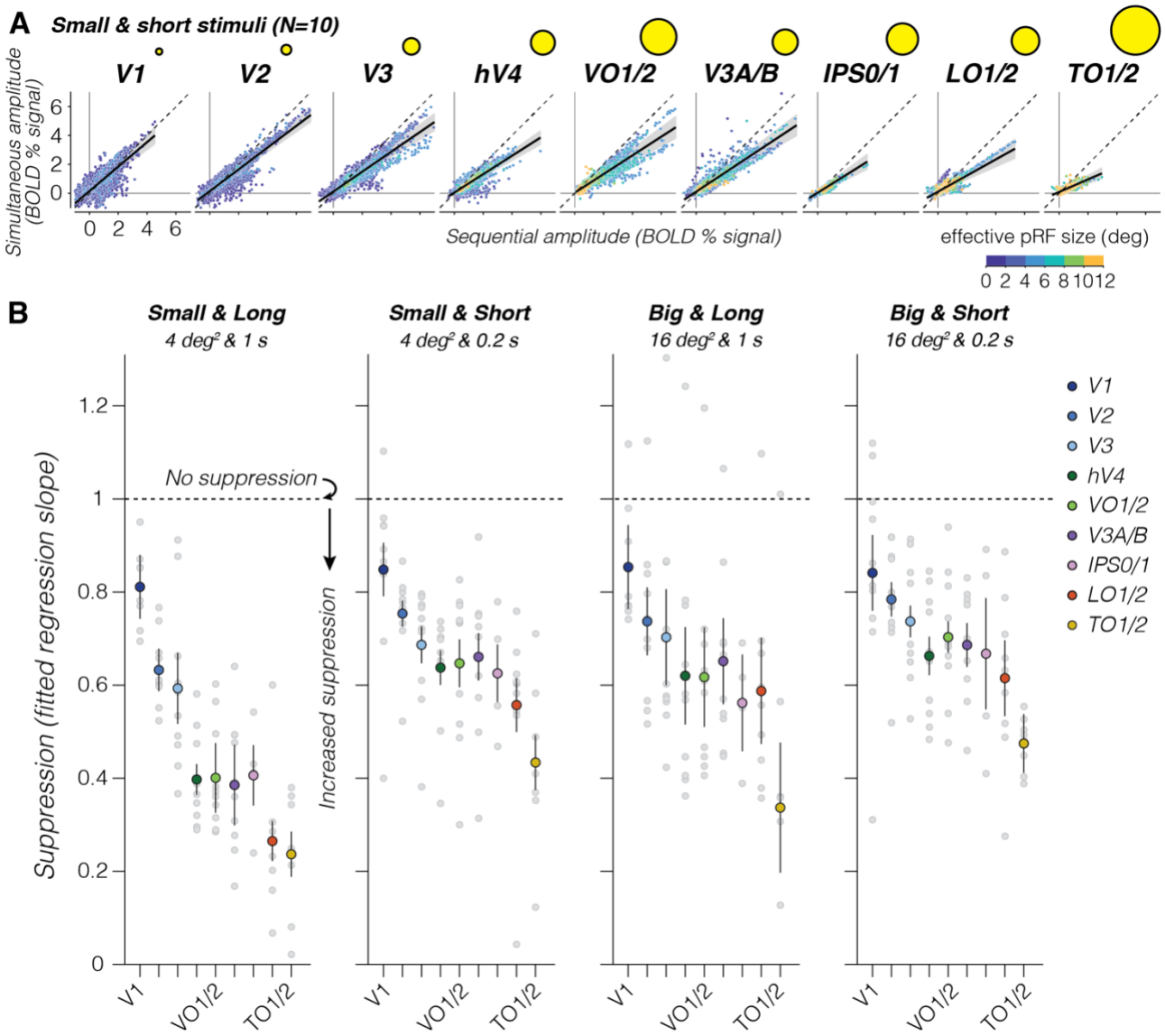

Figure 4. Simultaneous suppression increases up the visual hierarchy. (A) Average sequential vs simultaneous BOLD amplitude of individual voxels for small and short stimulus condition. Each point is a voxel, colored by effective pRF size estimated from the retinotopy data. Each panel shows data of all 10 participants. *Black solid line:* LMM fit (average across participants). *Dashed line*: identity line. *Shaded area:* $CI_{95\%}$ across participants. *Yellow circles:* illustration of average pRF size per area, ranging from 1° in V1 to 7.8° in TO1/2. **(B) Suppression levels for each stimulus condition and visual area.** Slopes are derived from

LMM fit to simultaneous vs sequential average BOLD amplitude data from all 10 participants, for each visual area. A slope of 1 indicates no suppression. Smaller slopes indicate larger suppression. *Large colored dots:* Group average of a visual area. *Error bars*: SEM across participants. *Light gray dots:* Individual participant slopes (random effects). Early visual areas are in blue colors (V1: indigo. V2: dark blue. V3: light blue), ventral visual areas in green colors (hV4: dark green. VO1/2: light green), dorsal visual areas are in purple colors (V3A/B: purple. IPS0/1: pink), and lateral visual areas are in warm colors (LO1/2: red. TO1/2: yellow).

The increasing suppression levels across the visual hierarchy are in line with our prediction that simultaneous suppression will be stronger in visual areas that have larger pRF sizes. This relationship is evident at the level of entire visual areas (**Fig 4B**), but not across voxels within an area (**Fig 4A**). Within an area, we find similar suppression levels for voxels with pRFs that drastically vary in size (e.g., VO1/2), yet their level of suppression is predicted by a single line. Thus, while pRF size is an important predictor of simultaneous suppression at the level of an entire visual area, our data suggest that by itself, summation within pRFs that vary in size is insufficient to explain different suppression levels observed across stimulus conditions. Together, these results reveal robust simultaneous suppression at the individual voxel level that depends both on pRF size alongside stimulus size and timing parameters.

3.4 A spatiotemporal pRF modeling framework to predict simultaneous suppression at the single voxel level

To gain insight into the stimulus-driven computations that give rise to different levels of simultaneous suppression at the voxel level, we developed a computational framework that predicts the neural population response in each voxel from its pRF given the frame-by-frame stimulus sequence of the SEQ-SIM experiment (**Fig 5**). To capture the brief nature of the stimuli and the neural response, both stimulus sequence and predicted pRF responses have millisecond resolution. This neural pRF response is then convolved with the hemodynamic response function (HRF) to predict the voxel's BOLD response and downsampled to 1 second resolution to match the fMRI acquisition (**Fig 5A**). Crucially, for each voxel, we use a single pRF model and the stimulus sequence of the entire SEQ-SIM experiment to predict its time series across all stimulus conditions at once. For all tested pRF models, spatial parameters of each voxel's pRF are identical and estimated from the independent retinotopy experiment (**Fig 1C**).

We tested three pRF models. First, a compressive spatiotemporal pRF model (CST[41]) (**Fig 5B**) to quantitatively examine if and to what extent compressive spatiotemporal summation within pRFs can predict simultaneous suppression across all stimulus manipulations. The CST pRF model contains three spatiotemporal channels that have the same spatial pRF (2D Gaussian) but different neural temporal impulse response functions (IRFs): a sustained, on-transient, and off-transient

channel that captures stimulus duration, onsets, and offsets; neural IRFs use default temporal pRF parameters from Stigliani et al.[32]. These spatiotemporal filter outputs are rectified and subjected to a compressive static nonlinearity, which produces subadditive spatiotemporal summation for both sustained and transient channels.

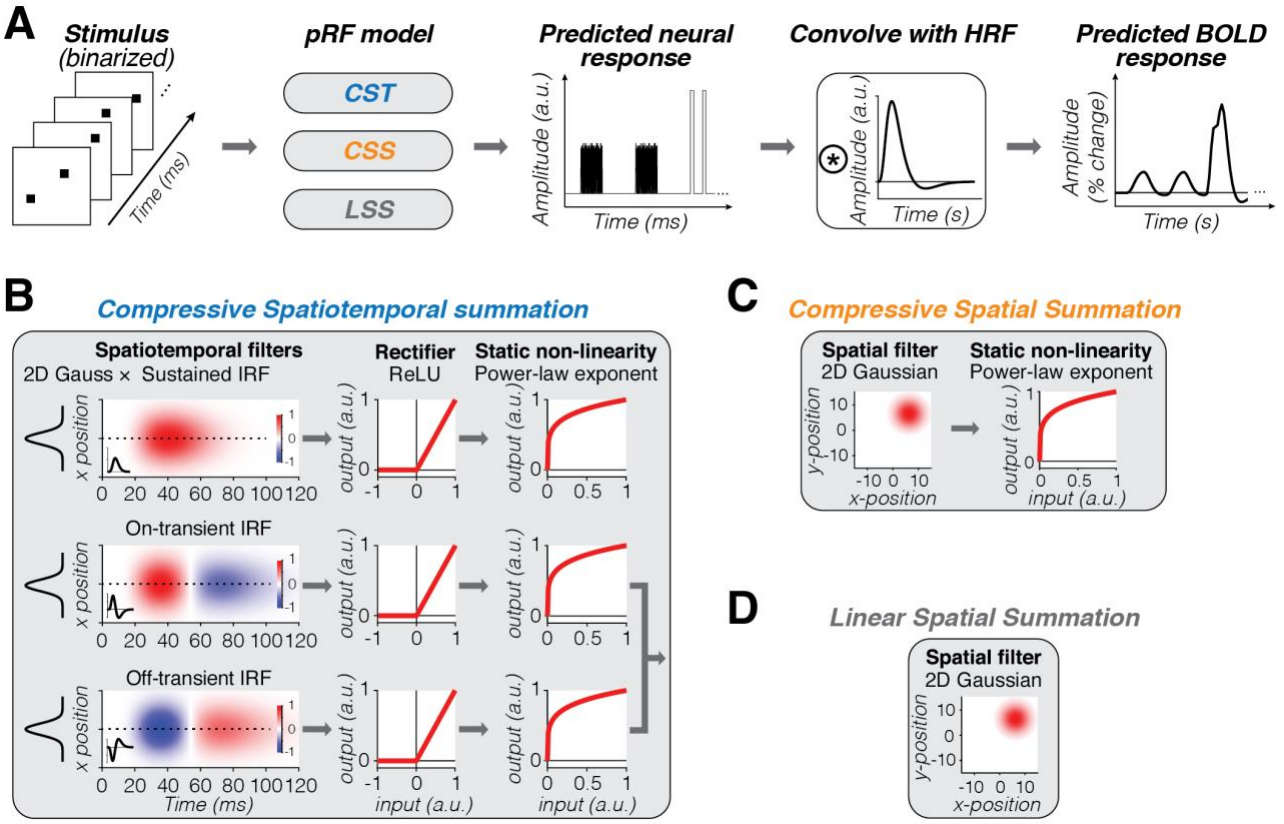

Figure 5. Computational modeling framework. (A) Model overview. *From left to right:* Given a binarized stimulus sequence and pRF model, the neural response is predicted at millisecond time resolution. This neural response is convolved with hemodynamic response function (HRF) to predict the BOLD response. After the convolution with the HRF, data are downsampled to 1-s resolution (TR in SIM-SEQ experiment). **(B-D) Tested pRF models.** For each voxel, spatial pRF parameters are identical for all models and estimated from the retinitopy experiment (Fig 1C). Both CSS and LSS models sum linearly over time. For simulated pRF model predictions, see Supplementary Fig 2. **(B) Compressive Spatiotemporal summation (CST)**[41]. Temporal pRF parameters are default parameters from Stigliani et al.[32]. Static power-law exponent parameter (<1) is the same for all three spatiotemporal channels and fitted to each voxel's SEQ-SIM data. The overall predicted BOLD response by the CST model is the weighted sum of the sustained and combined transient channel. **(C) Compressive spatial summation (CSS)**[22]. 2D Gaussian followed by a static compressive nonlinearity (exponent <1, estimated from retinotopy data). **(D) Linear spatial summation (LSS)**[17]. LSS pRFs sum linearly across space and time by computing the dot product between the binarized stimulus frame and the 2D Gaussian pRF.

Second, a compressive spatial summation pRF model (CSS[22]) (**Fig 5C**) to quantitatively test if subadditive spatial summation alone can explain simultaneous suppression. The CSS model has

a 2D Gaussian followed by a compressive static nonlinearity and is successful in predicting spatial subadditivity in voxels with larger pRFs beyond V1.

Third, a linear spatial summation pRF model (LSS[17]) (**Fig 5D**) to quantitatively test if small voxels that show little to no simultaneous suppression, such as those in V1, can be predicted by linear summation in space and time. The LSS pRF contains a 2D Gaussian for each voxel and sums stimulus input linearly over time and space. This model was also used as a benchmark for higher-level visual areas and to validate our experimental design, because linear summation of stimuli in paired SEQ-SIM conditions should not result in simultaneous suppression.

3.5 Comparing pRF model performance in predicting observed SEQ-SIM data

For each voxel, we generate three predicted BOLD responses, one for each tested pRF model (CST, CSS, LSS; see **Supplementary Fig 2** for example pRF model predictions). We fit each model using split-half cross-validation, resulting in a cross-validated variance explained (cv-R^2) for each voxel. This provides a principled and unbiased way to test the hypotheses.

For our example, small V1 pRF, both spatial models (LSS and CSS) predict the same BOLD response for sequential and simultaneous pairs (**Fig 6A**, bottom and middle rows). This is because the pRF covers only one small square, and consequently, spatial summation is identical across SIM and SEQ presentations. Comparing predictions to data, both LSS and CSS models capture the voxel's response to long stimulus conditions, but underpredict the voxel's response for short stimulus conditions, resulting in the same cross-validated variance explained (cv-R^2) of 43% for this V1 voxel. In comparison, the CST pRF model best captures the response pattern across all stimulus conditions (cv-R^2=52%), predicting no suppression and larger BOLD amplitudes for short than long stimulus conditions (**Fig 6A**, top row).

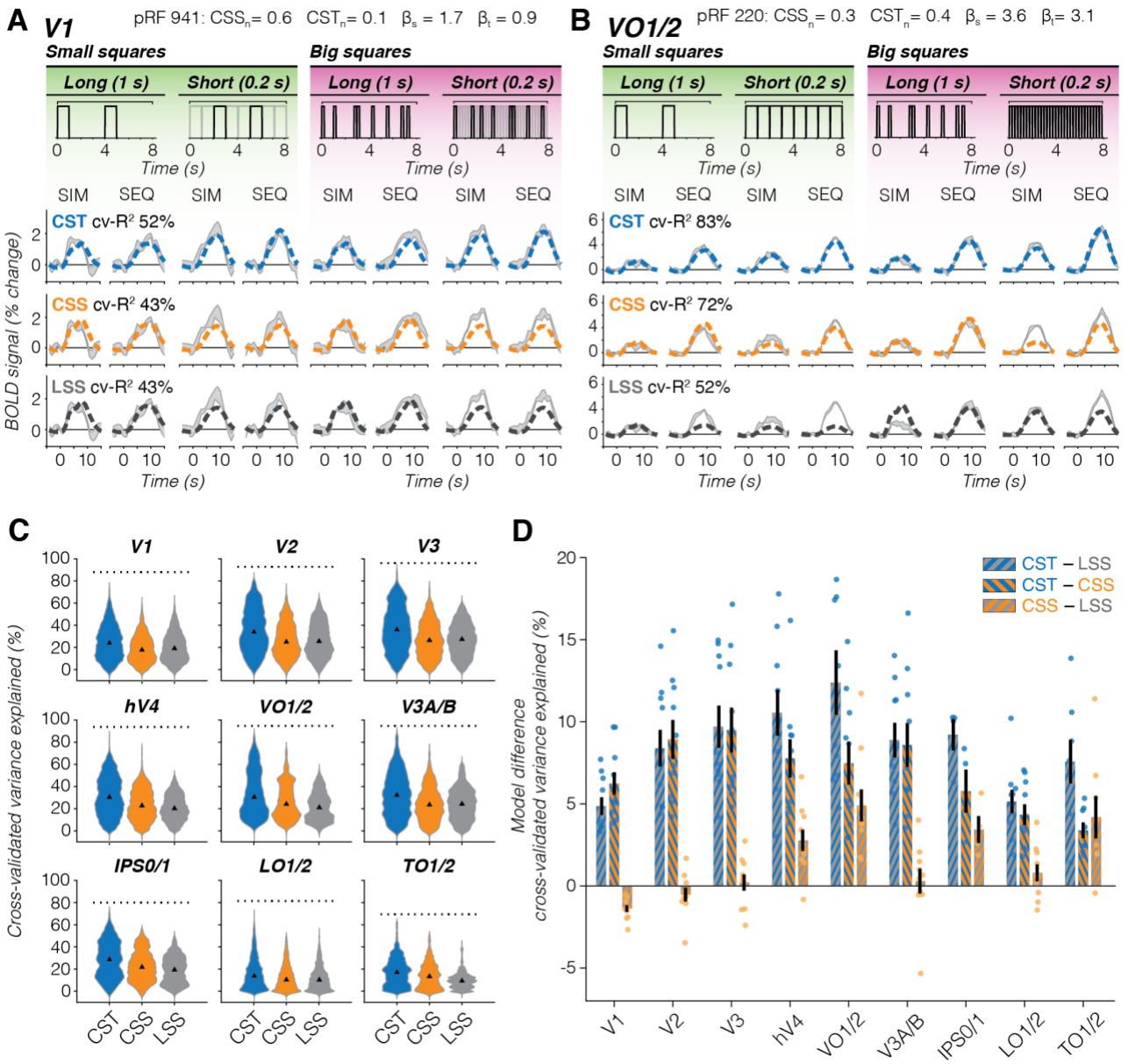

Figure 6. Comparison of pRF model performance. (A) V1 example voxel. *Gray shaded area:* Average ± SEM voxel time series. Data are from the same voxel as in Fig 2A repeated for each row. PRF model fits are shown in dashed lines. Split-half cross-validated variance explained (cv-R^2) is computed by fitting the predicted time series to the average of odd runs and applying the modelfit to the average of even runs and vice versa. *Blue:* Compressive spatiotemporal summation model (CST, top row). *Orange:* Compressive spatial summation model (CSS, middle row). *Black:* Linear spatial summation model (LSS, bottom row). **(B) VO1/2 example voxel.** Data are from the same voxel as in Fig 3A repeated for each row. Same color scheme as panel A. **(C) Distribution of voxel-level cross-validated variance explained for each pRF model, all 10 participants.** *Triangle:* median. *Dotted line:* noise ceiling computed from max split-half reliability across participants. *Blue:* CST. *Orange*: CSS. *Gray:* LSS. Since number of voxels vary per participant and visual area, we assure equal contribution of each participant by resampling data 1000x of each participant's visual area. **(D) Pairwise model comparison for each visual area.** *Bars:* show average across participants of the voxelwise difference in cv-R^2 between two pRF models. *Error bars:* SEM across participants. *Individual dots:* average difference for each participant. *Blue-gray:* CST vs LSS. *Blue-orange:* CST vs CSS. *Orange-gray:* CSS vs LSS.

When pRFs are large and cover multiple stimuli, like the example VO1/2 voxel, the LSS pRF model predicts larger responses for big than small squares, slightly higher responses for long than short presentations, and identical responses for sequential and simultaneous pairs. As such, it fails to predict the observed simultaneous suppression in all conditions (**Fig 6B**, bottom row). On the other hand, the CSS pRF model predicts simultaneous suppression because of spatial subadditivity, as well as a modest increase in response with stimulus size (**Fig 6B**, middle row). Like the LSS model, the CSS model predicts slightly larger responses for the long than short presentations of a given sequence type (SIM/SEQ). Consequently, the CSS model predicts simultaneous suppression well for the long presentations across stimulus sizes, but overpredicts simultaneous suppression for short presentations. In contrast, the CST pRF model best predicts all stimulus conditions for this example voxel: it shows simultaneous suppression, slightly larger response for big vs small stimulus sizes, and larger responses for short vs long presentation timings (**Fig 6B**, top row).

Across all voxels and visual areas, we find that the CST pRF model best predicts our data (**Fig 6C,D**). The CST model explains more cv-R^2 than LSS and CSS pRF models and approaches the noise ceiling in V3 and higher-level visual areas (**Fig 6C**, dotted line). A two-way repeated measures ANOVA with revealed significant effects of pRF model ($F(2)=2.6\times10^{3}$, $p<10^{-209}$) and ROI ($F(8)=3.4\times10^{3}$, $p<10^{-209}$) on cv-R^2, as well as a significant interaction between pRF model and ROI ($F(2,8)=65$, $p<2.8\times10^{-209}$). On average, the increase in cv-R^2 for the CST model compared to the other models ranges from ~5% in V1 to ~14% in VO1/2 (**Fig 6D**) and is significant in each visual area (**Supplementary Table 3,** post-hoc Bonferroni-corrected t-tests). Beyond early visual cortex, the CSS model outperforms LSS, but in V1 the LSS model slightly (+1.4%) and significantly ($p<2.7\times10^{-8}$) explains more variance than the CSS model. These results suggest that V1 voxels largely sum linearly in space, but nonlinearly in time. However, across the visual hierarchy, compressive spatiotemporal summation provides a more comprehensive explanation of the empirical data.

3.6 What pRF components drive the observed simultaneous suppression?

To understand the underlying neural computations that generate simultaneous suppression, we used pRF models to predict the level of simultaneous suppression in each voxel and condition of the SEQ-SIM experiment. Then, we compared the model-based simultaneous suppression level against the observed suppression (**Fig 7**, shaded gray bars).

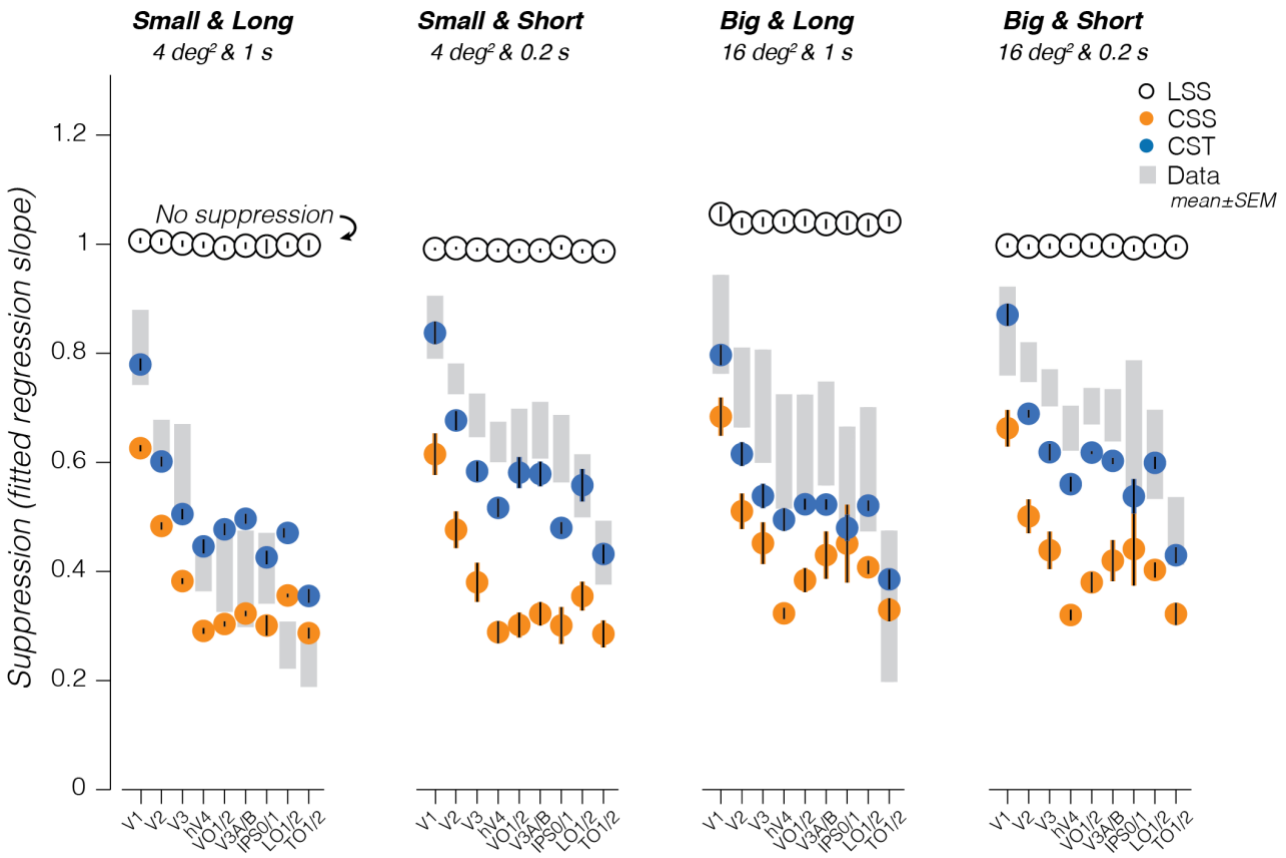

Figure 7. Model-based prediction of simulateneous suppression vs observed simulateneous suppresion. *Shaded gray bars:* Observed suppression levels in data, mean ± SEM across participants (same as Fig 4B). *Black open circles*: Linear spatial summation (LSS) pRF model; *Orange filled circles:* Compressive spatial summation (CSS) pRF model; *Blue filled circles:* Compressive spatiotemporal (CST) summation. Model-based points and errorbars show average and SEM across all 10 participants.

The CST model best captures simultaneous suppression across visual areas and stimulus conditions as its predictions are largely within the range of data variability (**Fig 7**, compare blue circles to shaded gray bars). Specifically, the CST model predicts (i) progressively increasing simultaneous suppression across visual hierarchy, (ii) stronger suppression for longer than shorter presentation timings for squares of the same size, and (iii) weaker suppression for bigger than smaller squares of the same timing.

The CSS model captures the progressively stronger simultaneous suppression across visual hierarchy and the observed simultaneous suppression for the long stimuli in a few visual areas (V3A/B, IPS0/1, and TO1/2), but fails to predict suppression for short stimuli and generally overpredicts the level of suppression (**Fig 7,** orange circles). In other words, the CSS model predicts much stronger simultaneous suppression levels than observed, as model points are consistently below the data. This overprediction is largest for short presentation timings in early (V1-V3) and

ventral visual areas (hV4 and VO1). One reason for this mismodeling error is that the CSS model does not encode visual transients: it predicts stronger simultaneous suppression for small than big sizes but predicts similar simultaneous suppression for long and short presentations of the same square size.

Finally, and as expected, the LSS model does not predict simultaneous suppression altogether. This is because the LSS model sums visual inputs linearly in space and time, and we designed our experiment such that each square is shown for the same duration and location in sequential and simultaneous conditions. Therefore, the LSS model predicts the same responses for sequential and simultaneous stimulus pairings and consequently no suppression (**Fig 7**, black open circles). For the big and long squares, the LSS model predicts slightly higher responses for simultaneous vs sequential presentations. We attribute this to our experimental design, which has different inter-stimulus-intervals of individual squares between sequential and simultaneous blocks, see *Methods – LSS pRF model*). Together, these model comparisons suggest that accounting for spatiotemporal nonlinearities rather than just spatial nonlinearities is necessary for predicting simultaneous suppression across a variety of spatiotemporal stimulus conditions.

What intrinsic pRF components drive the observed simultaneous suppression? Examining the CST model parameters reveals that simultaneous suppression depends on pRF size, compressive exponent, as well as contributions from both sustained and transient temporal channels (**Fig 8**). Visual areas with larger pRF sizes tend to show stronger simultaneous suppression levels (smaller slopes, Pearson's correlation r=-0.72, $CI_{95\%}$=-0.81–0.59, p<0.0001) (**Fig 8A**). Likewise, visual areas with stronger compression (smaller CST pRF exponent parameters) are linked to stronger simultaneous suppression levels (Pearson's r=0.65, $CI_{95\%}$=0.50–0.76, p<0.0001) (**Fig 8B**). Both pRF size and compression increase from early to higher-level visual areas, for example, along the lateral pathway: V1 through V3 followed by LO and TO. Indeed, V1 has the smallest pRF sizes and least compression (CST_n=0.71), whereas TO1/2 has the largest pRFs and strongest compression (CST_n=0.36). Lastly, we find that across visual areas, both sustained and transient channels contribute to predicting single voxel BOLD responses, as their β-weights are similar (no significant difference in β-weights across channels) (**Fig 8C**). These results indicate that both sustained and transient channels are needed to predict simultaneous suppression across different stimulus size and timing conditions.

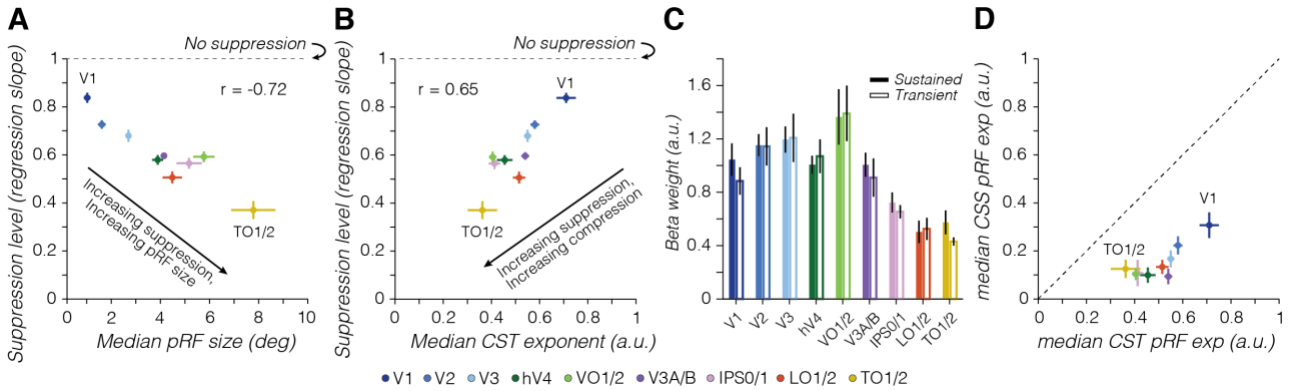

Figure 8. Simulateneous suppression depends on pRF size, compressive exponent, and contributions from both sustained and transient channels. In all panels: *dots/bars* show average across 10 participants. *Error bars:* SEM across 10 participants. **(A) Simultaneous suppression level vs median pRF size. (B) Simultaneous suppression level vs median CST pRF exponent.** For effective size and exponent pRF parameters, we first computed the median across pRFs of a visual area for each participant, as compressive exponent values in V1 and V2 voxels are not normally distributed (see Supplementary Fig 3), then we calculated the average median value across participants. Pearson's correlation (*r*) is computed using individual participant data. **(C) Average β-weights of sustained and transient channels in CST pRF model.** Beta weights are averaged first within a participant's visual area, to then average across participants per visual area. *Colored bars:* Sustained channel. *White bars:* Combined transient channel. Differences between sustained and transient channels are not significant. **(D) Median exponent pRF parameters for CSS vs CST model.** Dashed line indicates equality line.

Because the static nonlinearity in each CST pRF is applied to the output of spatiotemporal channels, the compression is of spatiotemporal nature and cannot be separated across spatial and temporal dimensions. Nevertheless, we can gain insight into the different contributions of spatial versus spatiotemporal compression by comparing the exponent across the CST and CSS pRF models. We find that across all visual areas, the CSS model predicts consistently higher compression (smaller exponent) than the CST model (**Fig 8D**). This overly strong compression by the CSS model likely explains its mismodeling of the short stimuli conditions where it predicts too much suppression (**Fig 7**). Overall, these results suggests that both spatial and temporal nonlinearities are necessary to account for the observed simultaneous suppression, and ultimately interact, resulting in a reduced spatiotemporal compression parameter.

4 Discussion

Simultaneous suppression is a decades-old, yet perplexing neurophysiological phenomenon: Why is the response to multiple stimuli presented simultaneously substantially lower compared to the response to the same stimuli presented sequentially? Here, we combined a new experimental design, varying stimulus size and presentation timing, with an innovative spatiotemporal pRF modeling framework to elucidate the stimulus-driven computations that give rise to simultaneous suppression in individual voxels. Our results show that the level of simultaneous suppression depends not only on the spatial overlap between stimuli and the pRF, but also on the timing of stimuli and the number of visual transients. Furthermore, we find that compressive (subadditive) spatiotemporal computations by pRFs are necessary to predict simultaneous suppression in each voxel across the visual hierarchy, and across various experimental conditions. These findings suggest that a stimulus-driven compressive spatiotemporal computation by pRFs generates simultaneous suppression and necessitate a rethinking of the neural mechanisms involved in simultaneous suppression.

4.1 Rethinking the neural mechanisms of simultaneous suppression

By investigating simultaneous suppression under a computational lens, measuring and predicting each voxel's pRF response independently, we provide a mechanistic explanation on how the spatial overlap between the stimulus and pRF drives simultaneous suppression at the single voxel level. This confirms the longstanding hypothesis that the overlap between the receptive field and stimuli matters[6,10,13]. Additionally, we show that increasing simultaneous suppression up the visual hierarchy is predicted by both the progressive increase in pRF size and the spatiotemporal compression strength.

Crucially, we are able to explain a wide range of simultaneous suppression levels by stimulus-driven computations within pRFs alone, which necessitates a rethinking of the neural processing underlying simultaneous suppression. Thus, we propose a new idea that simultaneous suppression is a consequence of simple, stimulus-driven spatiotemporal computations rather than a result of stimuli competing for limited neural resources within receptive fields, and prioritized by task demands. As our computational framework uses a stimulus-referred encoding model, it has predictive power. This allows future research to make new predictions about suppression levels for any stimulus sequences. The framework is also modular and can be expanded to computationally operationalize the effects of stimulus content, context, and task demands on simultaneous suppression.

4.2 Simultaneous suppression increases up the visual processing hierarchy, and depends on stimulus size and timing

Consistent with previous work[6,7,10,13], we find that simultaneous suppression increases up the visual hierarchy and is particularly strong in ventral visual areas (hV4 and VO1/2). Notably, we find that not only stimulus size and location, but also stimulus timing and number of visual transients affect the level of simultaneous suppression: for stimuli of the same size, longer timings (1 s) with fewer transients generated stronger suppression levels than shorter timings (0.2 s) with more transients. In contrast, many prior studies[6,10-13] used a single duration (0.25 s) similar to our short stimuli, for which we find weaker levels of simultaneous suppression. This may explain why we find moderate levels of suppression in V1 voxels despite having small pRFs; a result not reported previously. Another possibility is that we include all pRFs that overlap the stimuli, including small pRFs that partially overlap multiple squares. This differs from electrophysiology studies where stimuli are optimized to completely overlap with single neurons' receptive fields[7-9]. Moreover, we quantified simultaneous suppression in each voxel rather than an entire ROI[6,10-13], which may also explain differences across studies.

4.3 Compressive spatiotemporal computations within pRFs can explain simultaneous suppression across visual cortex

We compared three pRF models in our computational framework (LSS[17], CSS[22], and CST[41]) to test whether compressive spatial summation or compressive spatiotemporal summation better predict the simultaneous suppression. Overall, the CST pRF model provides a comprehensive explanation for simultaneous suppression across voxels spanning the ventral, dorsal, and lateral visual processing streams, stimuli varying in size, and brief presentations durations (0.2-1s) well below the temporal resolution of fMRI. We note that the high CST model performance across all visual areas is not a given, as different models could have better predicted certain visual areas or processing streams.

Spatial pRF models captured some, but not all aspects of the observed simultaneous suppression. For example, LSS pRFs predict the absence of simultaneous suppression in small V1 voxels and CSS pRFs predict lower responses for simultaneously vs sequentially presented stimuli, outperforming the LSS model beyond V1. However, LSS and CSS model were developed for stimulus durations and timings that evoke BOLD responses that approximately sum linearly in time. Hence, these models are limited because they do not account for visual transients. This is not only a limitation of the spatial pRF models we tested (LSS and CSS), but of any other pRF model that sums linearly over the stimulus duration, such as center-surround pRFs[23,43] or linear spatiotemporal

pRF models[44]. Likewise, we believe other mathematical forms of subadditive spatiotemporal summation could predict simultaneous suppression similarly to the CST model (e.g., a delayed normalization spatiotemporal pRF model[41]).

While the CST pRF model outperforms the LSS and CSS models by predicting simultaneous suppression across stimuli size and timing, it did not capture all spatiotemporal nonlinearities. For instance, for small and long stimuli, the CST model overpredicts suppression in early visual areas, but underpredicts suppression in higher-level areas. Future research may improve CST model performance by optimizing parameters of both neural and hemodynamic temporal impulse response functions (IRFs) in each voxel[41], and incorporating additional temporal nonlinearities, such as an exponential response decay[34,36].

We are not the first to consider temporal aspects of BOLD responses in models of the human visual system. Prior studies have suggested other hemodynamic[45,46] and neural[27,31-34,44] IRFs to capture BOLD temporal nonlinearities (see review [47]). Notwithstanding the success of these models, only the recent development of a compressive spatiotemporal pRF model[41] with a neural IRF in units of visual degrees and milliseconds provided us with the opportunity to examine what subadditive spatiotemporal computations contribute to simultaneous suppression for the following reasons. First, a successful model needs to account for neural nonlinearities. We believe that the observed nonlinearities are of neural rather than hemodynamic origin, as electrocorticography and single unit recordings show that neural responses to brief visual stimuli evoke strong visual transients and are nonlinear[34]. In a recent study, we have shown that implementing such neural nonlinearities in a computational model rather than optimizing hemodynamic responses is necessary to predict BOLD temporal nonlinearities to brief stimuli as in the present study[41]. Second, to capture visual transients in rapid succession, the model requires neural IRFs with millisecond precision and 50-200 ms response window rather than 1-4s window as afforded by hemodynamic models[44,46]. Third, the model also requires a spatial pRF. While prior studies have modeled neural IRFs with millisecond time resolution[27,31-34], without a spatial component these models are unable to predict differences in responses to one vs multiple stimuli covering a pRF.

4.4 Compressive spatiotemporal summation as a general computational mechanism in the visual system

A key insight from our study is that both increasing pRF size and stronger spatiotemporal compression contribute to increasing levels of simultaneous suppression up the visual processing hierarchy. This insight complements prior work[6,10,48] which proposed that the progressive increase in receptive field size causes stronger simultaneous suppression in higher-level areas.

Increasing receptive field size and compression from early to higher-level visual areas have been interpreted as increasing summation windows that enhance invariance both in space[20,22,23,49,50] and time[24-26,29,31,33,36]. This aligns with the idea that spatial and temporal compression of visual information share a similar processing strategy[33] and suggests that compressive spatiotemporal summation may be a general computational principle in visual cortex.

What may be the role of compressive spatiotemporal summation? Little is known regarding to the role of compressive spatiotemporal summation outside of motion processing[51-54]. One possibility is that increasing compressive spatiotemporal summation generates representations that encode complex shape and motion information that unfolds over time[55]. This may be useful for binding different views of novel objects during unsupervised learning (associated with ventral stream functions[56,57]) or for perceiving complex visual dynamics, actions, and social interactions (associated with lateral stream functions[58-60]). Another possibility is that spatiotemporal compression within pRFs may enable neurons to prioritize novel visual information[5,61]. This may be beneficial for visual search[1,2] or short-term visual working memory by converting redundant visual information into a more efficient representation[62]. However, spatiotemporal compression may also limit visual processing capacity, affecting downstream cognitive processes such as worse memory for simultaneously vs sequentially-presented items[63]. Thus, an important future direction is characterizing and computationally linking visual capacity and simultaneous suppression.

In sum, our empirical data and voxel-wise pRF modeling approach, call for a rethinking of the neural mechanisms that drive simultaneous suppression and suggest that suppression is a byproduct of compressive spatiotemporal computations. These findings provide exciting new opportunities to computationally understand how stimulus content, context, and task demands affect simultaneous suppression and visual processing capacity more broadly.

5 Methods

5.1 Participants

Ten participants (6 female, ages 22-53 years, M = 30.1 years, SD = 8.7 years) with normal or corrected-to-normal vision participated in a retinotopy and SEQ-SIM fMRI experiment. Participants gave written informed consent, were compensated for their time, and all procedures were approved by the Stanford Internal Review Board on Human Subjects Research.

5.2 Stimuli & experimental design

Stimuli were generated using MATLAB (MathWorks, MA, USA) and PsychToolbox[64] on an Apple MacBook Pro laptop. Images were presented using an Eiki LC-WUL100L projector (Eiki International, Inc., CA, USA) on a rear-projection screen via two large mirrors placed at the back of the MRI scanner bed. The projected image had a resolution of 1920x1080 pixels, resulting in a field-of-view of ~38x24°, and refresh rate of 60 Hz. The display was calibrated using a linearized lookup table.

Retinotopy experiment. Participants completed four 3.4-minute runs, where bar stimuli cropped from colorful cartoons traversed across a 24x24° circular aperture (Toonotopy[42]). Cartoon images inside the bar changed randomly at 8 Hz. The bar swept in 12 discrete steps, 2-s per bar position, for 4 orientations (0°, 45°, 90°, 135°) and 2 motion directions for each orientation. Observers fixated on a central dot (diameter = 0.12°) and pressed a button every time the fixation dot changed color (semi-random intervals, 6–36 s). Due to a coding error, button presses were only recorded for 3 participants, who performed at ceiling (M = 98.7% correct, SD = 1.2%).

SEQ-SIM experiment. Participants completed eight ~5.5-minute runs (except for participant S5, completing six runs), where 8 squares were presented sequentially or simultaneously while fixating: 4 squares in the lower right quadrant and 4 squares in the upper left quadrant. Both sequential and simultaneous conditions used two presentation timings (short: 0.2 s and long: 1 s) and two sizes (small: 2x2° and big: 4x4°), resulting in eight conditions.

Stimuli: Squares were randomly cropped from colorful cartoons and placed on a mean luminance gray background. To ensure square stimuli would elicit responses in visual cortex, squares with little to no contrast were excluded (normalized root mean square contrast across pixels < 10%). The content of individual squares differed for each trial and quadrant, and never repeated within a run. Within a quadrant, squares had a 2-by-2 layout with a 0.82° gap between them, centered at ~7.1° eccentricity ([x,y] = [5°,5°]). Both sizes used identical gap and eccentricity, such that 4 small squares extended horizontally and vertically from 2.59° to 7.41°, and big squares extended from

0.59° to 9.41°. The lower right and upper left quadrant had the same square locations but mirrored horizontally and vertically.

Experimental Design: Stimuli were shown in ~8 s blocks, interspersed by 12-s blank periods. Each run started with a 6-s countdown and 12-s blank and ended with a 12-s blank. Each condition was repeated four times in a pseudo-randomized order across two runs. The block order, as well as individual square presentation within a block, differed across runs. Each participant was assigned a unique pair of runs, which were repeated four times (three for participant S5) within the experiment with different square content (see example: https://osf.io/7rqf4).

Sequential and simultaneous conditions had 8 trials per block for short stimuli and 2 trials per block for long stimuli. We used different trial-per-block ratios such that short and long conditions had a similar total block duration while the number of visual transients quadrupled (16 vs 64)—matching the increase between small and big square sizes (4 vs 16 deg^2). In a sequential trial, the four squares in each quadrant appeared one at a time, in random order, with a 33-ms inter-stimulus-interval (ISI) between squares. In a simultaneous trial, all four squares in a quadrant appeared at once for the same duration and location followed by a mean luminance gray display to match duration of a sequential trial.

Block onsets and stimulus conditions were identical across quadrants, but timing and order of individual square appearances were independently determined per quadrant. In simultaneous blocks with long stimulus presentations, stimuli in the first trial were presented at block onset to match sequential blocks. Stimuli of the second trial were presented 4 s later to avoid 7-s gaps between stimuli within a block. In simultaneous blocks with short presentations, stimuli in the first trial were also locked to block onset, but onset of stimuli in the following 7 trials was randomized within a trial.

Task & Behavioral performance: Participants performed a 1-back letter RSVP task at fixation and pressed a button when a letter repeated (1/9 probability). The letters (diameter of ~0.5°) updated at 1.5 Hz, alternating between black and white colors, and randomly drawn from a predefined list ('A', 'S', 'D', 'F', 'G', 'H', 'J', 'K', 'B', 'P'). Participants had a 0.83-s response window after a letter appeared and performance was displayed after every run. Outside the scanner, participants did 1-minute practice runs until they reached at least 70% correct before starting the experiment. In the scanner, participants performed the task well (M=88% correct, SD=8.2%), ranging from 68–95%, and average false alarm rate of 2%. These behavioral data are confirmed by steady fixation in eye movement data (**Supplementary Fig 4**) and indicate that participants were fixating throughout experimental runs.

5.3 MRI data acquisition

Participant's structural and functional data were collected using a 3T GE Signa MR750 scanner located in the Center for Cognitive and Neurobiological Imaging at Stanford University. Whole brain T1-weighted anatomy were acquired using a BRAVO pulse sequence (1 mm^3 isotropic, inversion time=450 ms, TE=2.912 ms, FA=12°), using a Nova 32-channel head coil. Functional data were collected using a Nova 16-channel coil, using a T2*-sensitive gradient echo planar imaging sequence (2.4 mm^3 isotropic, FoV=192 mm, TE=30 ms, FA=62°). EPI slice prescriptions were oblique, roughly perpendicular to the calcarine sulcus. Retinotopy experiment used a TR of 2000 ms and 28 slices. SEQ-SIM experiment used a TR of 1000 ms and 14 slices. A T1-weighted inplane image (0.75x0.75x2.4 mm) was collected with the same coil and slice prescription as the functional scans to align functional and anatomical scans.

Left eye gaze data of 9 participants were continuously recorded in each SEQ-SIM run at 1000 Hz using an EyeLink 1000 (SR Research Ltd., Osgoode, ON, Canada). Eye position calibration and validation was conducted before the first run, using a 5-point grid. We could not collect eye gaze data in one participant due to constraints in the mirror setup. Four participants were excluded prior to analysis due to excessive measurement noise. Analysis details for eye gaze data are in the *Supplemental Material* above **Supplementary Fig 4**.

5.4 MRI data analysis

5.4.1 Reproducible computation and code sharing

Data analyses were conducted in MATLAB (R2020b) and for FreeSurfer's auto-segmentation[65] (v6.0; http://surfer.nmr.mgh.harvard.edu/). Data and analysis code are publicly available at https://osf.io/rpuhs/, https://github.com/VPNL/simseqPRF, and https://github.com/VPNL/spatiotemporalPRFs.

5.4.2 Preprocessing

Whole-brain T1-weighted scans were aligned to the AC-PC line using SPM12 (https://github.com/spm/spm12) and auto-segmented with FreeSurfer's *recon-all* algorithm. Functional data were slice-time corrected, motion corrected, drift corrected, converted to percent signal change using the *Vistasoft* toolbox (https://github.com/vistalab/vistasoft). Participants' functional scans were aligned with the inplane to their whole brain anatomy scan, using a coarse, followed by a fine 3D rigid body alignment (6 DoF) using the *alignvolumedata_auto* toolbox

(https://github.com/cvnlab/alignvolumedata). The first 8 (SEQ-SIM) or 6 (Retinotopy) volumes of each functional scan were removed to avoid data with unstable magnetization.

Retinotopy analysis. Retinotopy runs were averaged and analyzed with Vistasoft's compressive spatial summation pRF model (CSS)[22] using a 2-stage optimization (coarse grid-fit, followed by fine search-fit). For each voxel, this resulted in 2D Gaussian pRF with center coordinates (x_0, y_0) in degrees, pRF standard deviation (σ) in degrees and pRF static nonlinearity exponent (CSS_n) ranging from 0.01 to 1. To avoid pRFs that are not visually responsive, we selected pRFs with R^2 ≥20% in the retinotopy experiment, similar to previous pRF publications[42,66].

Defining visual areas. Spatial pRF parameters were converted to polar angle and eccentricity maps and projected to participant's native cortical surface using nearest neighbor interpolation. Visual field maps were used to define the following visual areas: V1, V2, and V3[67], hV4 and VO1/2[68], LO1/2 and TO1/2[69], and V3A/B and IPS0/1[70].

Defining ROIs and selecting voxels. For each visual area, we selected voxels with pRFs centers within the circumference of the big squares in the SEQ-SIM experiment, that is, within an 8.82x8.82° square located 0.59° to 9.41° from display center in both x- and y-dimensions in each quadrant. From these voxels, we used those with corresponding data from the SEQ-SIM experiment. Overall, we obtained data in most participants' visual areas, except 6 participants who had insufficient coverage of IPS0/1 and 2 participants who had insufficient coverage of TO1/2, due to fewer slices in the SEQ-SIM experiment.

SEQ-SIM analysis. We excluded voxels with a split-half reliability <10% to filter out those voxels with little to no visual response. Excluded voxels were mostly from V1 and V2, with small pRFs that fell in between stimuli or on the border of stimuli. The two unique SEQ-SIM runs were concatenated for each repeat. When applying split-half cross-validation for model fitting, the 4 concatenated runs were split into two odd and two even runs, and averaged within each half.

5.5 pRF modeling framework

Our modeling framework contained three pRF models: (i) LSS, to test linear spatial summation[17], (ii) CSS, to test compressive spatial summation[22], and (iii) CST, to test compressive spatiotemporal summation[41]. Both LSS and CSS models linearly sum over the temporal duration of the stimulus.

Each model's input is a 3D binarized stimulus sequence, pixels by pixels (in visual degrees) by time (milliseconds). Each pRF is applied to each frame of the stimulus sequence to predict the neural pRF response. For each model, this neural response is then convolved with a canonical hemodynamic response function (HRF) (double-gamma SPM default) and downsampled to the fMRI

acquisition TR. This results in a predicted BOLD response for the entire stimulus sequence. For each pRF that overlapped stimuli in SEQ-SIM experiment, predictions were computed for each unique 5.5-min run, and then concatenated for the two unique runs. Importantly, concatenated runs contained all 8 stimulus conditions, requiring each model to predict all conditions simultaneously.

LSS pRF model. The LSS model has a 2D Gaussian pRF with an area summing to 1, computing the dot product between the 2D Gaussian and stimulus sequence to predict the neural response. This model sums inputs linearly in visual space and time, and typically predicts the same BOLD response for sequential and simultaneous trials. For longer stimulus durations, the LSS model occasionally predicts larger responses for simultaneous than sequential, due to a difference in square ISI between the two condition blocks. Specifically, the randomized square onset causes sequential ISIs to range from 1–7s, which by chance can be longer than the fixed 4-s simultaneous ISI—especially when pRFs are small and overlap a single square. When this occurs, LSS predicts the BOLD responses accumulate less in the sequential than simultaneous block.

CSS pRF model. The CSS model is similar to the LSS model but applies a static power-law nonlinearity exponent CSS_n between 0.1–1. The spatial nonlinearity is compressive when CSS_n<1.

CST pRF model. The CST model contains three spatiotemporal channels. Each channel has an identical spatial pRF as the LSS model, combined with a sustained, on-transient, or off-transient neural temporal impulse response function (IRF). For each channel, we apply the dot product between the spatial pRF and the stimulus sequence, which output is then convolved with the neural temporal IRF with millisecond time resolution. Each channel's response then goes through the same rectified linear unit (ReLU, where $f(x) = \max(0, x)$). The rectified response is subjected to a static power-law nonlinearity, where the CST exponent parameter (CST_n) is bound between 0.1–1, compressing the output. Predicted neural responses for sustained and the summed transient channels are then convolved with the HRF. The voxel's response is the weighted sum of the two (β_S, β_T) time series.

The sustained, on-transient, and off-transient IRFs are as described in ref[41], and are identical across voxels, using default V1 parameters from ref[31]. The sustained IRF is monophasic gamma function that peaks between 40-50 ms (time constant parameter τ=4.93 ms, exponent parameter n=9). The on-transient IRF is the difference of two gamma functions, the sustained IRF and a second gamma function (τ=4.93 ms, n=10, time constant ratio parameter κ=1.33), resulting in a biphasic function that generates a brief response at stimulus onset. The off-transient IRF is identical to the on-transient IRF but with opposite sign, generating a response at stimulus offset. The area under the sustained IRF is normalized to sum to 1, and area under each transient IRF is sums to 0.

Fixed and optimized pRF parameters. Spatial pRF parameters were independently estimated from each participant's retinotopy experiment using the CSS pRF model, resulting in a pRF center (x_0, y_0), standard deviation (σ) and exponent (CSS_n) parameter for each voxel. The standard deviation and exponent parameter trade-off in the CSS model (see ref[22]), where $\frac{\sigma}{\sqrt{n}}$ approximates the effective pRF size: the standard deviation (σ) estimated with a linear pRF model (LSS, no spatial compression). Therefore, to reconstruct CSS pRFs. we use each voxel's estimated CSS parameters (x_0, y_0, σ, and exponent). To reconstruct LSS and CST pRFs, we use the same estimated pRF center (x_0, y_0), but for the standard deviation (σ) we use the effective pRF size.

The CST model had fixed parameters for the neural temporal IRFs and only optimized the CST_n using a grid-fit approach. Per pRF, the best fitting CST_n was determined by systematically evaluating goodness-of-fit of predicted time series with CST_n between 0.1–1 (0.05 steps) and selecting the CST_n resulting in the highest cross-validated R^2. We used a grid-fit instead of a search-fit optimization approach to avoid estimates getting stuck in a local minimum.

5.6 Model fitting

We fitted each voxel's pRF model prediction separately to data, using a split-half cross-validation procedure. The maximum height of predicted BOLD time series was normalized to 1 and we added a column of 1's to capture response offset. This resulted in two regressors (β_0, β_1) for LSS and CSS models, and three regressors (β_0, β_S, β_T) for CST. We used linear regression (ordinary least squares) to fit these regressors to the voxel's observed time series, separately for odd and even splits. To determine model goodness-of-fit (variance explained), we computed the cross-validated coefficient of determination (cv-R^2) by using the scaled predicted time series of one split to predict observed time series from the other split and vice versa (i.e., β-weights are fixed and not refitted). Cv-R^2 values and β-weights were averaged across split halves for each voxel. Split-half reliability across runs was used as the noise ceiling.

To check whether CST model performance could be inflated by the extra regressor, we also computed cross-validated adjusted-R^2, which penalizes goodness-of-fit for the number of time points and explanatory variables. The adjusted-R^2 values were almost numerically identical to R^2 and did not significantly affect our results nor statistical comparisons.

5.7 Linear mixed model

To quantify simultaneous suppression, we fitted a linear mixed model (LMM) to all participant's voxels within a visual area with MATLAB's *fitlme.m*, using the maximum likelihood fitting method. This LMM

predicted the average simultaneous BOLD response of each voxel as a function of the average sequential BOLD response, for each stimulus condition (fixed interaction effect), allowing for a random intercept and slope per participant and stimulus condition (random interaction effect):

Equation 1: $SIM\ ampl \sim 1 + SEQ\ ampl \times Condition + (1 + SEQ\ ampl \times Condition \mid Participant)$

where *SIM ampl* and *SEQ ampl* are a matrix (nr voxels x 4) with continuous values, *Condition* is a categorial vector (1 x 4), and *Participant* is the group level for the random effects (10 participants).

This LMM captured our data well (mean R^2 = 90%, SD = 6.6%), with V1: 86%, V2: 94%, V3: 94%, hV4: 92%, VO1/2: 97%, V3A/B: 95%, IPS0/1: 88%, LO1/2: 85%, and TO1/2: 76% variance explained. We tested this LMM to three alternative LMMs: (i) mean sequential amplitude as a fixed factor (no condition interaction effect) with one random intercept per participant, (ii) a fixed interaction effect with a single intercept per participant, identical for each stimulus condition, and (iii) a fixed interaction effect with a random participant intercept for each condition. Despite having more degrees of freedom (45) than the alternative LMMs (4, 10, and 19), the main LMM was a better fit to the data as it had a significantly higher log-likelihood than alternative LMMs, and lower AIC and BIC for each visual area (F-test $p < 0.00001$) (**Supplementary Fig 5**).

5.8 Summarizing results

BOLD time series. Both observed and predicted run time series were averaged across split-halves and segmented into 23-TR time windows. These time windows spanned from 4 s pre-block onset, 8 s stimulus block, to 11 s post-block. For each voxel, we took the average time window and standard error of the mean (SEM) across 4 repeats.

Seq vs Sim BOLD amplitude. The average data and model time windows were summarized into 8 values per voxel (one per condition), by averaging the BOLD response within a 9-TR window centered on the peak, spanning from either 4–12s or 5–13s after stimulus block onset. These values were used in LMMs and scatter plots. We used a variable start per condition and visual area because the BOLD accumulation rate differed. The start was determined by averaging (data or model) time windows across voxels within a visual area and condition, into a “grand mean” time window and finding the first TR after block onset where the BOLD response exceeded 10% of the total cumulative sum. This averaging window was applied to all voxels within a visual area.

Simultaneous suppression effects. We summarized LMM results for each condition and visual area as line fits with 95%-confidence intervals ($CI_{95\%}$) using the slope and intercept of the individual participants (**Fig 2B** and **3B**) or average across participants (**Fig 4A**). For **Fig 4B**, we summarized the simultaneous suppression level using the average slope and SEM across participants. For **Fig 8**, we first average slopes across conditions within a participant, and then average slopes across participants (± SEM).

PRF parameters. We resampled pRF size, CSS_n, CST_n, and CST β_S and β_T 1000x with replacement within a participant's visual area, because the number of voxels varied across areas and participants. For pRF size and exponents, we report the median resampled parameter for each participant and visual area because the V1 and V2 CST_n were not normally distributed (see **Supplementary Fig 3**). CST β_S and β_T were normally distributed; hence, we report the average resampled beta weights per participant and visual area. For group results, we report the average (± SEM) across participants' mean or median resampled parameter value, for each visual area.

5.9 Statistical analyses

To quantify differences in LMM regression slopes, we ran a two-way repeated measures ANOVA with factors visual area and stimulus conditions across participants. To quantify differences in pRF model cv-R^2, we ran a two-way repeated measures ANOVA with factors pRF model and visual area across voxels of all participants and visual areas. For both ANOVA results, if there was a main effect (p<0.05), we used Bonferroni-corrected post-hoc multiple comparison t-tests to evaluate differences between pRF models, or visual area and stimulus condition. We used Pearson's correlation r to quantify the relationship between participant slopes averaged across conditions and effective pRF size or CST_n across visual areas.

6 References

1 Duncan, J. The locus of interference in the perception of simultaneous stimuli. *Psychol Rev* **87**, 272-300 (1980).

2 Scharff, A., Palmer, J. & Moore, C. M. Evidence of fixed capacity in visual object categorization. *Psychon Bull Rev* **18**, 713-721 (2011). https://doi.org:10.3758/s13423-011-0101-1

3 Pelli, D. G., Palomares, M. & Majaj, N. J. Crowding is unlike ordinary masking: distinguishing feature integration from detection. *J Vis* **4**, 1136-1169 (2004). https://doi.org:10.1167/4.12.12

4 Luck, S. J. & Vogel, E. K. The capacity of visual working memory for features and conjunctions. *Nature* **390**, 279-281 (1997). https://doi.org:10.1038/36846

5 Desimone, R. & Duncan, J. Neural mechanisms of selective visual attention. *Annu Rev Neurosci* **18**, 193-222 (1995).

6 Kastner, S., De Weerd, P., Desimone, R. & Ungerleider, L. G. Mechanisms of directed attention in the human extrastriate cortex as revealed by functional MRI. *Science* **282**, 108-111 (1998). https://doi.org:10.1126/science.282.5386.108

7 Reynolds, J. H., Chelazzi, L. & Desimone, R. Competitive mechanisms subserve attention in macaque areas V2 and V4. *J Neurosci* **19**, 1736-1753 (1999). https://doi.org:10.1523/JNEUROSCI.19-05-01736.1999

8 Miller, E. K., Gochin, P. M. & Gross, C. G. Suppression of visual responses of neurons in inferior temporal cortex of the awake macaque by addition of a second stimulus. *Brain Res* **616**, 25-29 (1993). https://doi.org:10.1016/0006-8993(93)90187-r

9 Recanzone, G. H., Wurtz, R. H. & Schwarz, U. Responses of MT and MST neurons to one and two moving objects in the receptive field. *Journal of neurophysiology* **78**, 2904-2915 (1997). https://doi.org:10.1152/jn.1997.78.6.2904

10 Kastner, S. *et al.* Modulation of sensory suppression: implications for receptive field sizes in the human visual cortex. *Journal of neurophysiology* **86**, 1398-1411 (2001). https://doi.org:10.1152/jn.2001.86.3.1398

11 Beck, D. M. & Kastner, S. Stimulus context modulates competition in human extrastriate cortex. *Nat Neurosci* **8**, 1110-1116 (2005). https://doi.org:10.1038/nn1501

12 McMains, S. A. & Kastner, S. Interactions of top-down and bottom-up mechanisms in human visual cortex. *J Neurosci* **31**, 587-597 (2011). https://doi.org:10.1523/JNEUROSCI.3766-10.2011

13 Kim, N. Y., Pinsk, M. A. & Kastner, S. Neural Basis of Biased Competition in Development: Sensory Competition in Visual Cortex of School-Aged Children. *Cerebral cortex* **31**, 3107-3121 (2021). https://doi.org:10.1093/cercor/bhab009

14 Usher, M. & Niebur, E. Modeling the Temporal Dynamics of IT Neurons in Visual Search: A Mechanism for Top-Down Selective Attention. *J Cogn Neurosci* **8**, 311-327 (1996). https://doi.org:10.1162/jocn.1996.8.4.311

15 Deco, G. & Rolls, E. T. Neurodynamics of biased competition and cooperation for attention: a model with spiking neurons. *Journal of neurophysiology* **94**, 295-313 (2005). https://doi.org:10.1152/jn.01095.2004

16 Maunsell, J. H. & Newsome, W. T. Visual processing in monkey extrastriate cortex. *Annu Rev Neurosci* **10**, 363-401 (1987). https://doi.org:10.1146/annurev.ne.10.030187.002051

17 Dumoulin, S. O. & Wandell, B. A. Population receptive field estimates in human visual cortex. *NeuroImage* **39**, 647-660 (2008). https://doi.org:10.1016/j.neuroimage.2007.09.034

18 Wandell, B. A. & Winawer, J. Computational neuroimaging and population receptive fields. *Trends Cogn Sci* **19**, 349-357 (2015). https://doi.org:10.1016/j.tics.2015.03.009

19 Hansen, K. A., David, S. V. & Gallant, J. L. Parametric reverse correlation reveals spatial linearity of retinotopic human V1 BOLD response. *NeuroImage* **23**, 233-241 (2004). https://doi.org:10.1016/j.neuroimage.2004.05.012

20 Press, W. A., Brewer, A. A., Dougherty, R. F., Wade, A. R. & Wandell, B. A. Visual areas and spatial summation in human visual cortex. *Vision Res* **41**, 1321-1332 (2001). https://doi.org:10.1016/s0042-6989(01)00074-8

21 Vanni, S. & Rosenstrom, T. Local non-linear interactions in the visual cortex may reflect global decorrelation. *J Comput Neurosci* **30**, 109-124 (2011). https://doi.org:10.1007/s10827-010-0239-2

22 Kay, K. N., Winawer, J., Mezer, A. & Wandell, B. A. Compressive spatial summation in human visual cortex. *Journal of neurophysiology* **110**, 481-494 (2013). https://doi.org:10.1152/jn.00105.2013

23 Aqil, M., Knapen, T. & Dumoulin, S. O. Divisive normalization unifies disparate response signatures throughout the human visual hierarchy. *Proc Natl Acad Sci U S A* **118** (2021). https://doi.org:10.1073/pnas.2108713118

24 Tolhurst, D. J., Walker, N. S., Thompson, I. D. & Dean, A. F. Non-linearities of temporal summation in neurones in area 17 of the cat. *Exp Brain Res* **38**, 431-435 (1980). https://doi.org:10.1007/BF00237523

25 Motter, B. C. Modulation of transient and sustained response components of V4 neurons by temporal crowding in flashed stimulus sequences. *J Neurosci* **26**, 9683-9694 (2006). https://doi.org:10.1523/JNEUROSCI.5495-05.2006

26 Hasson, U., Yang, E., Vallines, I., Heeger, D. J. & Rubin, N. A hierarchy of temporal receptive windows in human cortex. *J Neurosci* **28**, 2539-2550 (2008). https://doi.org:10.1523/JNEUROSCI.5487-07.2008

27 Horiguchi, H., Nakadomari, S., Misaki, M. & Wandell, B. A. Two temporal channels in human V1 identified using fMRI. *NeuroImage* **47**, 273-280 (2009). https://doi.org:10.1016/j.neuroimage.2009.03.078

28 Nishimoto, S. & Gallant, J. L. A three-dimensional spatiotemporal receptive field model explains responses of area MT neurons to naturalistic movies. *J Neurosci* **31**, 14551-14564 (2011). https://doi.org:10.1523/JNEUROSCI.6801-10.2011

29 Honey, C. J. *et al.* Slow cortical dynamics and the accumulation of information over long timescales. *Neuron* **76**, 423-434 (2012). https://doi.org:10.1016/j.neuron.2012.08.011

30 Mattar, M. G., Kahn, D. A., Thompson-Schill, S. L. & Aguirre, G. K. Varying Timescales of Stimulus Integration Unite Neural Adaptation and Prototype Formation. *Current biology : CB* **26**, 1669-1676 (2016). https://doi.org:10.1016/j.cub.2016.04.065

31 Stigliani, A., Jeska, B. & Grill-Spector, K. Encoding model of temporal processing in human visual cortex. *Proc Natl Acad Sci U S A* **114**, E11047-E11056 (2017). https://doi.org:10.1073/pnas.1704877114

32 Stigliani, A., Jeska, B. & Grill-Spector, K. Differential sustained and transient temporal processing across visual streams. *PLoS computational biology* **15**, e1007011 (2019). https://doi.org:10.1371/journal.pcbi.1007011

33 Zhou, J., Benson, N. C., Kay, K. N. & Winawer, J. Compressive Temporal Summation in Human Visual Cortex. *J Neurosci* **38**, 691-709 (2018). https://doi.org:10.1523/JNEUROSCI.1724-17.2017

34 Zhou, J., Benson, N. C., Kay, K. & Winawer, J. Predicting neuronal dynamics with a delayed gain control model. *PLoS computational biology* **15**, e1007484 (2019). https://doi.org:10.1371/journal.pcbi.1007484

35 Hendrikx, E., Paul, J. M., van Ackooij, M., van der Stoep, N. & Harvey, B. M. Visual timing-tuned responses in human association cortices and response dynamics in early visual cortex. *Nat Commun* **13**, 3952 (2022). https://doi.org:10.1038/s41467-022-31675-9

36 Groen, I. I. A. *et al.* Temporal dynamics of neural responses in human visual cortex. *J Neurosci* **42**, 7562-7580 (2022). https://doi.org:10.1523/JNEUROSCI.1812-21.2022

37 Maunsell, J. H., Nealey, T. A. & DePriest, D. D. Magnocellular and parvocellular contributions to responses in the middle temporal visual area (MT) of the macaque monkey. *J Neurosci* **10**, 3323-3334 (1990). https://doi.org:10.1523/JNEUROSCI.10-10-03323.1990

38 De Valois, R. L. & Cottaris, N. P. Inputs to directionally selective simple cells in macaque striate cortex. *Proc Natl Acad Sci U S A* **95**, 14488-14493 (1998). https://doi.org:10.1073/pnas.95.24.14488

39 Ray, S. & Maunsell, J. H. Different origins of gamma rhythm and high-gamma activity in macaque visual cortex. *PLoS biology* **9**, e1000610 (2011). https://doi.org:10.1371/journal.pbio.1000610

40 Jacques, C. *et al.* Corresponding ECoG and fMRI category-selective signals in human ventral temporal cortex. *Neuropsychologia* **83**, 14-28 (2016). https://doi.org:10.1016/j.neuropsychologia.2015.07.024

41 Kim, I., Kupers, E. R., Lerma-Usabiaga, G. & Grill-Spector, K. Characterizing spatiotemporal population receptive fields in human visual cortex with fMRI. *bioRxiv* **2023.05.02.539164** (2023). https://doi.org:https://doi.org/10.1101/2023.05.02.539164

42 Finzi, D. *et al.* Differential spatial computations in ventral and lateral face-selective regions are scaffolded by structural connections. *Nat Commun* **12**, 2278 (2021). https://doi.org:10.1038/s41467-021-22524-2

43 Zuiderbaan, W., Harvey, B. M. & Dumoulin, S. O. Modeling center-surround configurations in population receptive fields using fMRI. *J Vis* **12**, 10 (2012). https://doi.org:10.1167/12.3.10

44 DeSimone, K. & Schneider, K. A. Distinguishing Hemodynamics from Function in the Human LGN Using a Temporal Response Model. *Vision (Basel)* **3** (2019). https://doi.org:10.3390/vision3020027

45 Henson, R. N., Price, C. J., Rugg, M. D., Turner, R. & Friston, K. J. Detecting latency differences in event-related BOLD responses: application to words versus nonwords and initial versus repeated face presentations. *NeuroImage* **15**, 83-97 (2002). https://doi.org:10.1006/nimg.2001.0940

46 Lewis, L. D., Setsompop, K., Rosen, B. R. & Polimeni, J. R. Fast fMRI can detect oscillatory neural activity in humans. *Proc Natl Acad Sci U S A* **113**, E6679-E6685 (2016). https://doi.org:10.1073/pnas.1608117113

47 Polimeni, J. R. & Lewis, L. D. Imaging faster neural dynamics with fast fMRI: A need for updated models of the hemodynamic response. *Prog Neurobiol* **207**, 102174 (2021). https://doi.org:10.1016/j.pneurobio.2021.102174

48 Kastner, S. & Ungerleider, L. G. The neural basis of biased competition in human visual cortex. *Neuropsychologia* **39**, 1263-1276 (2001). https://doi.org:10.1016/s0028-3932(01)00116-6

49 Macevoy, S. P. & Epstein, R. A. Decoding the representation of multiple simultaneous objects in human occipitotemporal cortex. *Current biology : CB* **19**, 943-947 (2009). https://doi.org:10.1016/j.cub.2009.04.020

50 Rust, N. C. & Dicarlo, J. J. Selectivity and tolerance ("invariance") both increase as visual information propagates from cortical area V4 to IT. *J Neurosci* **30**, 12978-12995 (2010). https://doi.org:10.1523/JNEUROSCI.0179-10.2010

51 Adelson, E. H. & Bergen, J. R. Spatiotemporal energy models for the perception of motion. *J Opt Soc Am A* **2**, 284-299 (1985). https://doi.org:10.1364/josaa.2.000284

52 Watson, A. B. & Ahumada, A. J., Jr. Model of human visual-motion sensing. *J Opt Soc Am A* **2**, 322-341 (1985). https://doi.org:10.1364/josaa.2.000322

53 Heeger, D. J. Modeling simple-cell direction selectivity with normalized, half-squared, linear operators. *Journal of neurophysiology* **70**, 1885-1898 (1993). https://doi.org:10.1152/jn.1993.70.5.1885

54 Simoncelli, E. P. & Heeger, D. J. A model of neuronal responses in visual area MT. *Vision Res* **38**, 743-761 (1998). https://doi.org:10.1016/s0042-6989(97)00183-1

55 Russ, B. E., Koyano, K. W., Day-Cooney, J., Perwez, N. & Leopold, D. A. Temporal continuity shapes visual responses of macaque face patch neurons. *Neuron* **111**, 903-914 e903 (2023). https://doi.org:10.1016/j.neuron.2022.12.021

56 Wallis, G. & Bulthoff, H. Learning to recognize objects. *Trends Cogn Sci* **3**, 22-31 (1999). https://doi.org:10.1016/s1364-6613(98)01261-3

57 Zhuang, C. *et al.* Unsupervised neural network models of the ventral visual stream. *Proc Natl Acad Sci U S A* **118** (2021). https://doi.org:10.1073/pnas.2014196118

58 Pitcher, D. & Ungerleider, L. G. Evidence for a Third Visual Pathway Specialized for Social Perception. *Trends Cogn Sci* **25**, 100-110 (2021). https://doi.org:10.1016/j.tics.2020.11.006

59 Weiner, K. S. & Grill-Spector, K. Neural representations of faces and limbs neighbor in human high-level visual cortex: evidence for a new organization principle. *Psychol Res* **77**, 74-97 (2013). https://doi.org:10.1007/s00426-011-0392-x

60 Wurm, M. F. & Caramazza, A. Two 'what' pathways for action and object recognition. *Trends Cogn Sci* **26**, 103-116 (2022). https://doi.org:10.1016/j.tics.2021.10.003

61 Mruczek, R. E. & Sheinberg, D. L. Context familiarity enhances target processing by inferior temporal cortex neurons. *J Neurosci* **27**, 8533-8545 (2007). https://doi.org:10.1523/JNEUROSCI.2106-07.2007

62 Brady, T. F., Konkle, T. & Alvarez, G. A. Compression in visual working memory: using statistical regularities to form more efficient memory representations. *J Exp Psychol Gen* **138**, 487-502 (2009). https://doi.org:10.1037/a0016797

63 Ihssen, N., Linden, D. E. & Shapiro, K. L. Improving visual short-term memory by sequencing the stimulus array. *Psychon Bull Rev* **17**, 680-686 (2010). https://doi.org:10.3758/PBR.17.5.680

64 Brainard, D. H. The Psychophysics Toolbox. *Spat Vis* **10**, 433-436 (1997).

65 Dale, A. M., Fischl, B. & Sereno, M. I. Cortical surface-based analysis. I. Segmentation and surface reconstruction. *NeuroImage* **9**, 179-194 (1999). https://doi.org:10.1006/nimg.1998.0395

66 Poltoratski, S., Kay, K., Finzi, D. & Grill-Spector, K. Holistic face recognition is an emergent phenomenon of spatial processing in face-selective regions. *Nat Commun* **12**, 4745 (2021). https://doi.org:10.1038/s41467-021-24806-1

67 Smith, A. T., Singh, K. D., Williams, A. L. & Greenlee, M. W. Estimating receptive field size from fMRI data in human striate and extrastriate visual cortex. *Cerebral cortex* **11**, 1182-1190 (2001). https://doi.org:10.1093/cercor/11.12.1182

68 Witthoft, N. *et al.* Where is human V4? Predicting the location of hV4 and VO1 from cortical folding. *Cerebral cortex* **24**, 2401-2408 (2014). https://doi.org:10.1093/cercor/bht092

69 Amano, K., Wandell, B. A. & Dumoulin, S. O. Visual field maps, population receptive field sizes, and visual field coverage in the human MT+ complex. *Journal of neurophysiology* **102**, 2704-2718 (2009). https://doi.org:10.1152/jn.00102.2009

70 Swisher, J. D., Halko, M. A., Merabet, L. B., McMains, S. A. & Somers, D. C. Visual topography of human intraparietal sulcus. *J Neurosci* **27**, 5326-5337 (2007). https://doi.org:10.1523/JNEUROSCI.0991-07.2007

7 Supplementary Material

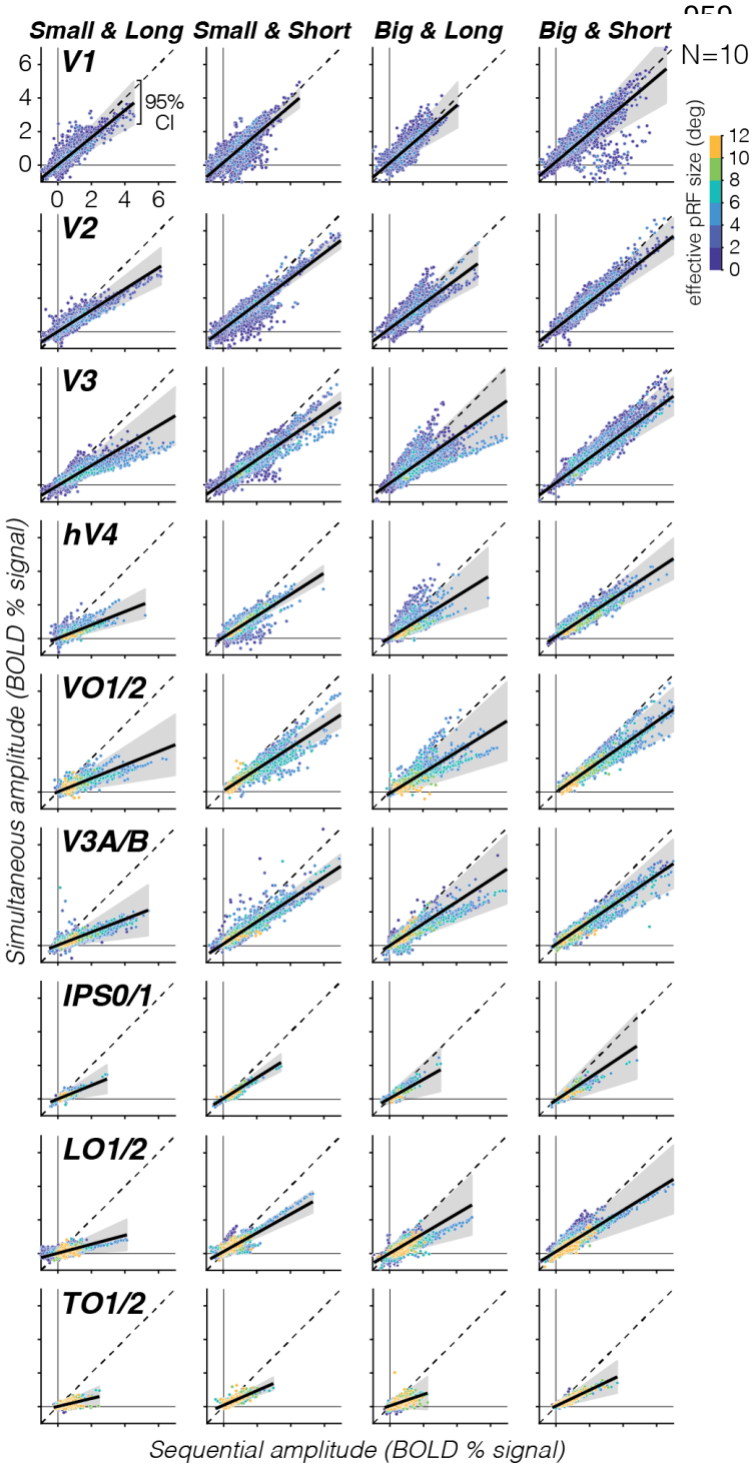

Supplementary Figure 1. Average sequential vs simultaneous BOLD amplitude of individual voxels for all stimulus condition. Each point is a voxel are colored by effective pRF size estimated from retinotopy data in six 2º non-overlapping bins. Each panel shows data of all 10 participants. *Black solid line:* average LMM slope across participants. *Shaded area:* 95%-confidence interval across participants. *Dashed line*: identity line, no suppression.

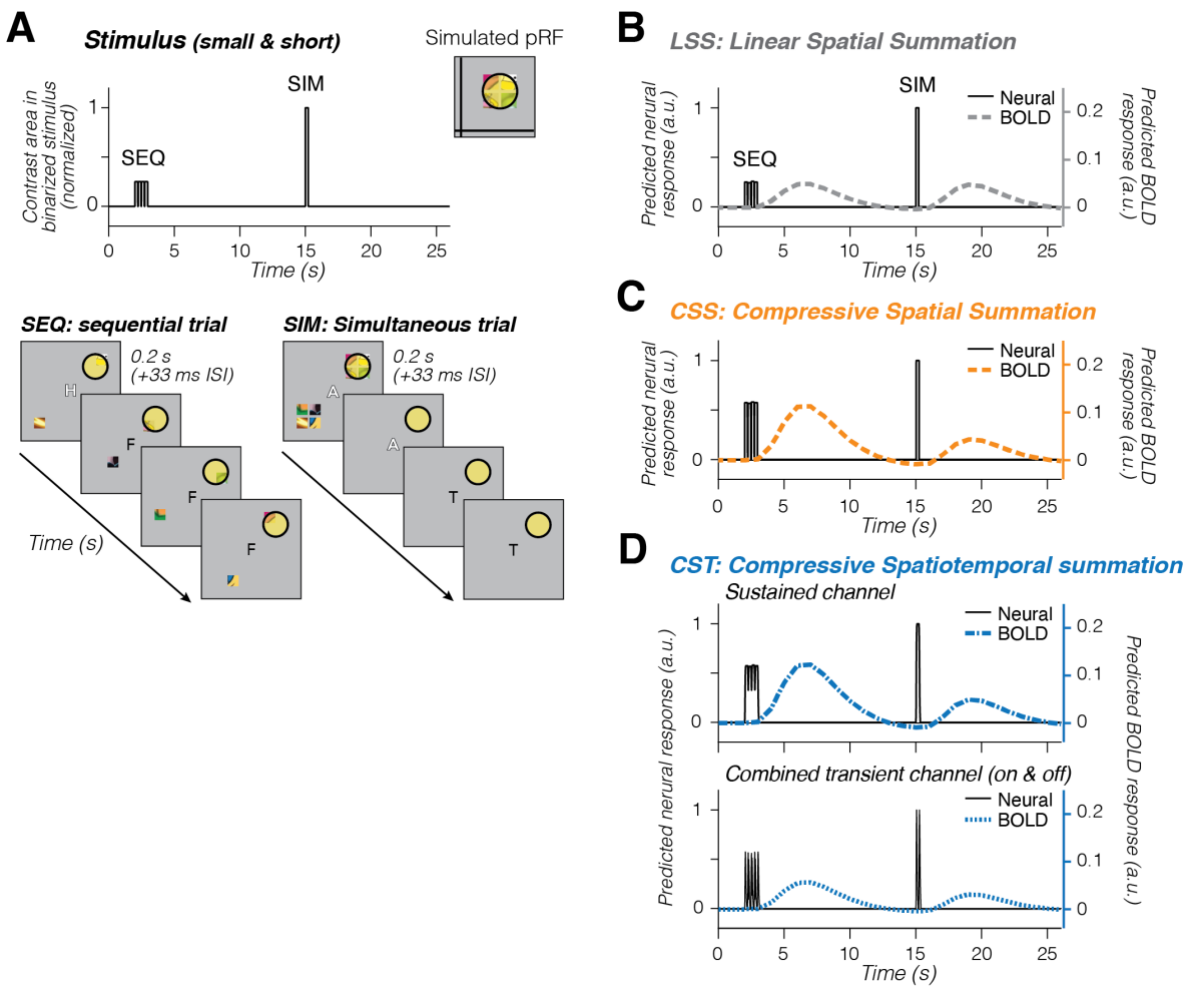

Supplementary Figure 2. Simulated pRF model predictions for a sequential trial followed by a simultaneous trial. Each model simulation uses a large pRF (see inset in A) that overlaps four small squares presented for 0.2 s (short square timing). **(A) Stimulus time course.** The stimulus' visual extent is represented as the total contrast area in a binarized stimulus frame, where pixels are summed across space for each time point and normalized to set the maximum contrast area to 1. Because each trial has 4 squares per quadrant, the contrast area for each square in the sequential trial (SEQ) is a fourth of the area when all squares are shown simultaneously (SIM). **(B-D) PRF model predictions.** *Black lines & left y-axis:* predicted neural response. *Colored lines & right y-axis:* predicted BOLD response. **(B) Linear spatial summation (LSS) pRF prediction (dashed gray)**. The LSS model sums stimulus input linearly over time and space. This linearity, combined with individual squares in simultaneous and sequential trials being matched in duration and location relative to the pRF, results in the LSS model predicting no simultaneous suppression. **(C) Compressive spatial summation (CSS) pRF prediction (dashed orange).** Due to the compressive static nonlinearity, the CSS model predicts simultaneous suppression when multiple squares (simultaneously) overlap with the pRF than when a single square (sequentially) overlaps the pRF. The CSS pRF model sums linearly in time and as individual square duration is matched between paired sequential and simultaneous conditions, it will not predict differences in response amplitude for short vs long stimulus presentation timings. **(D) Compressive spatiotemporal summation (CST) pRF prediction (blue)**. *Blue dot-dashed:* sustained spatiotemporal channel. *Blue dashed:* combined on- and off-transient spatiotemporal channel. By explicitly encoding neural temporal transients in milliseconds, the CST model predicts BOLD responses larger responses for many visual transients (SEQ) vs a few transients (SIM). The static nonlinearity produces additional subadditive spatiotemporal summation for both sustained and transient channels, including spatial subadditivity when multiple squares overlap the pRF. Consequently, both CST channels generate larger responses for sequential than simultaneous presentations.

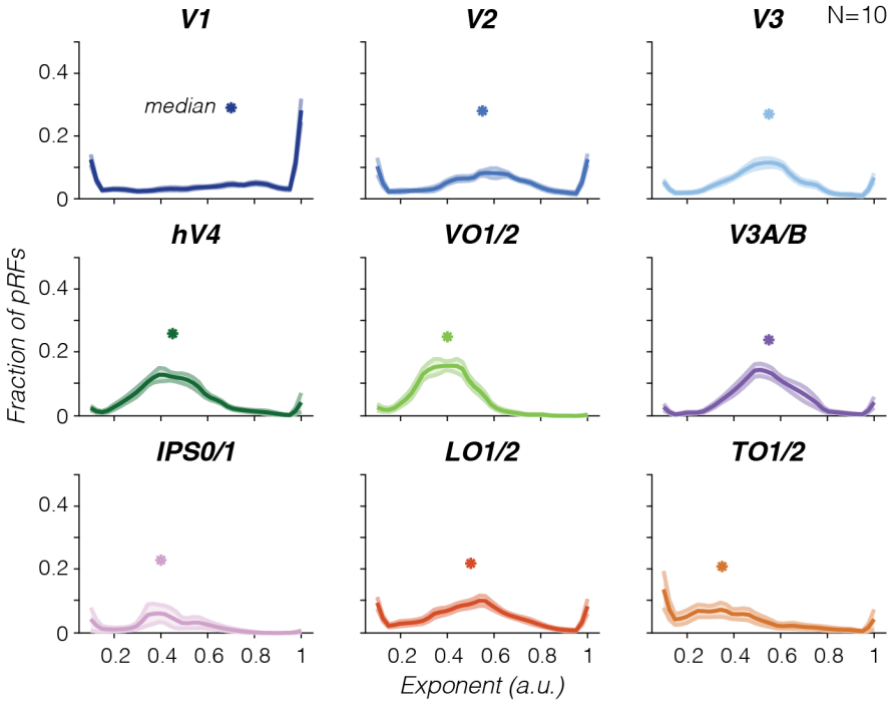

Supplementary Figure 3. Average CST pRF exponent parameter distributions. Distributions are computed by first resampling participants' data 1000x per ROI, then averaging distributions across participants. Both group average (line) and SEM (shaded area) of each ROI distribution are then upsampled 2x. *Asterisks:* median CST exponent value.

Eye movement analysis. Raw horizontal and vertical gaze position (deg) and velocity (deg/s) time series of 5 participants during SEQ-SIM fMRI experiment were preprocessed as follows. First, we removed time points occurring within -100 to 100 ms of blinks. Second, given large amounts of spatial noise, we used the Identification by Two-Means Clustering algorithm [1] to label robust fixation periods and their visual field location. If gaze locations jumped between two means due to noise, we recentered data to a single mean. Third, we removed time points (and surrounding 2 ms) if it had (i) a velocity larger than a typical saccade up to 8º (400 deg/s) [2], (ii) an absolute gaze location beyond stimulus display (radius = 10º), or (iii) a gaze position SD 2.5x larger than SD across horizontal and vertical time series. We excluded 7 runs with < 20% data, resulting in 32 runs total. We visualized participant's median and kernel density of gaze location across runs in visual space.

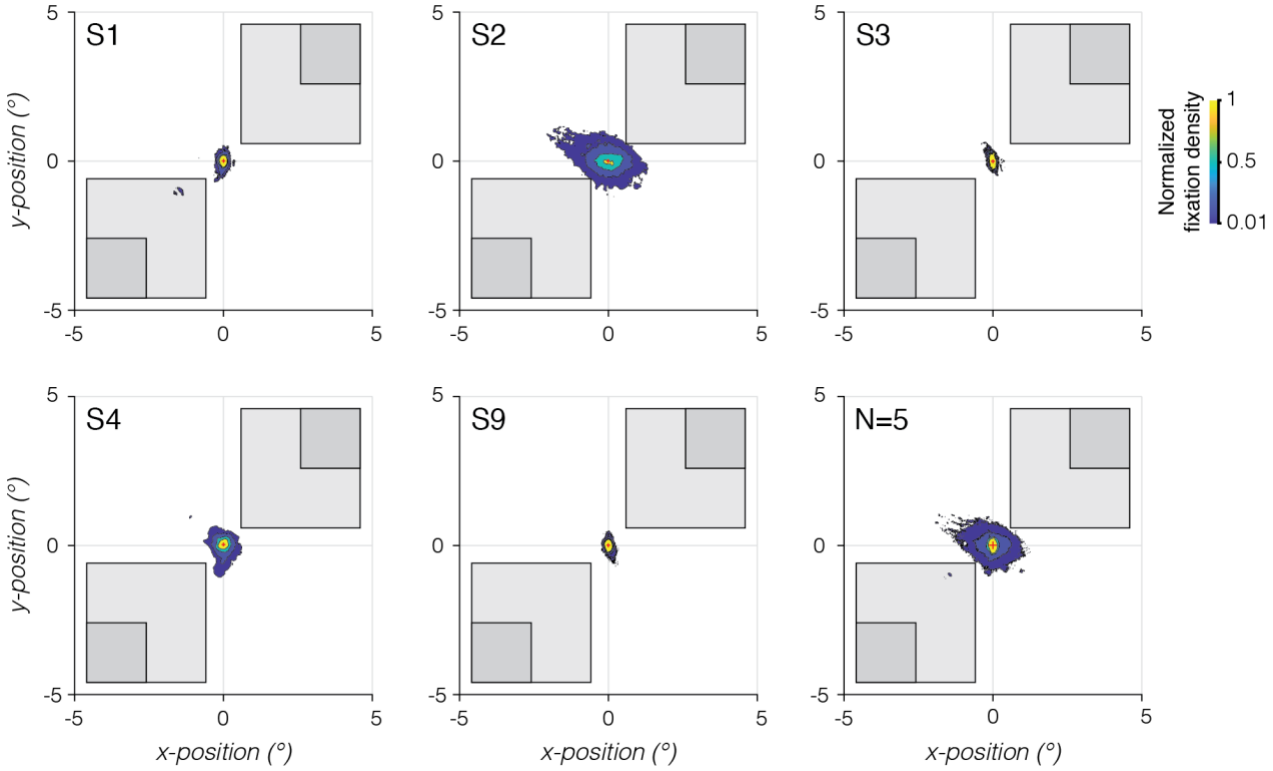

Supplementary Figure 4. Eye fixation locations during SEQ-SIM experiment. Normalized fixation density is shown for 5 participants (S1, S2, S3, S4, S9) and across all participants (N=5). *Red cross:* Median gaze location across runs. *Contour lines*: Density at 1st, 10th, 50th, 100th percentile, correspond to magenta, dark blue, green, and yellow sections. *Light gray squares:* Outlined location of large squares closest to fixation ([x,y]=[0,0]). *Dark gray squares:* Outlined location of small squares closest to fixation.

1. Hessels, R.S., et al., Noise-robust fixation detection in eye movement data: Identification by two-means clustering (I2MC). *Behav Res Methods* **49**(5), 1802-1823 (2017).
2. Smeets, J.B. and Hooge, I.T. Nature of variability in saccades. *J Neurophysiol* **90**(1), 12-20 (2003).

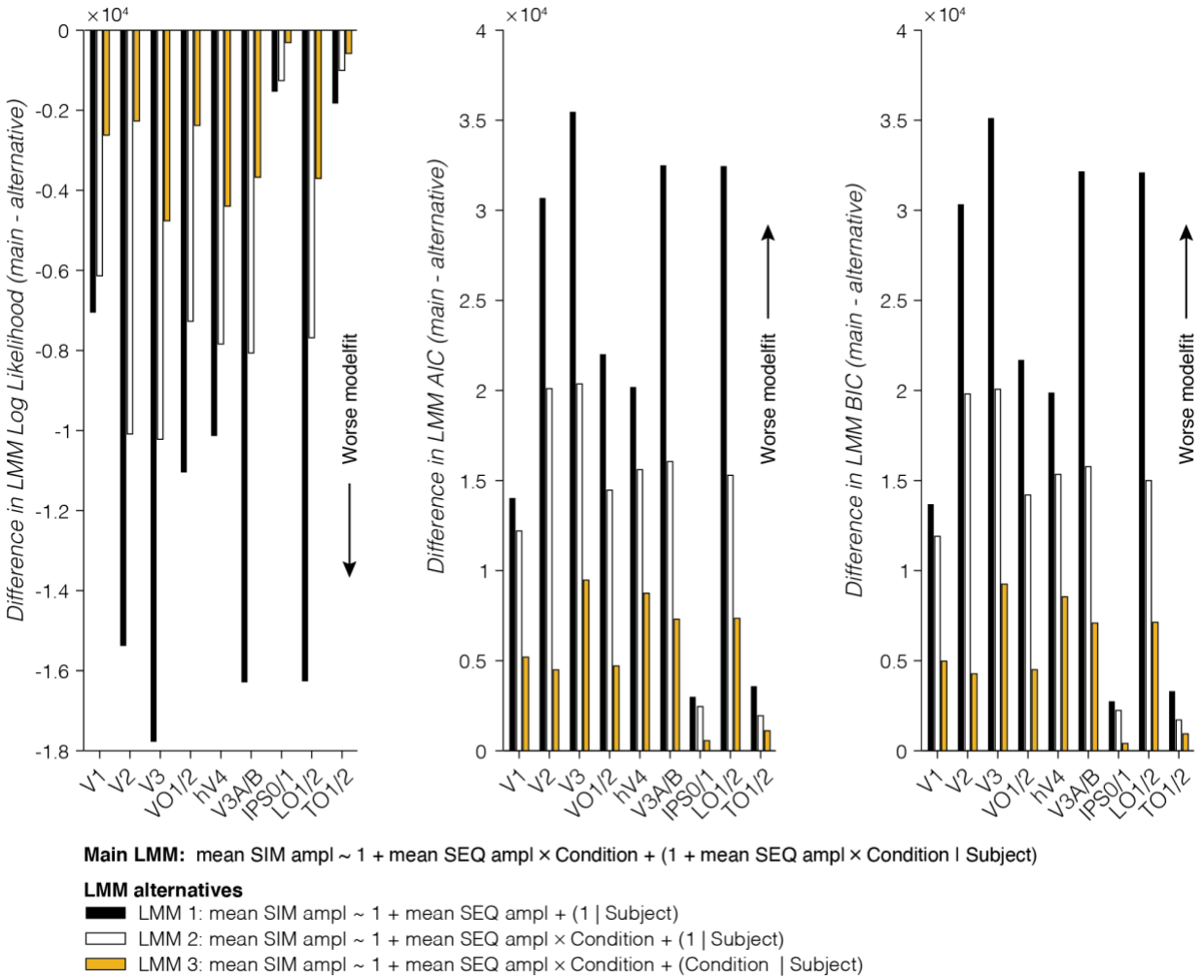

Supplementary Figure 5. Comparison of linear mixed models (LMMs). For each model comparison metric, we computed the difference between main LMM and alternative LMM. The main LMM fits the data better than all alternative LMMs, for each visual area, on each metric. *Right:* Difference in LMM log likelihood. *Middle:* Difference in LMM AIC. *Left:* Difference in LMM BIC. The main LMM uses a fixed intercept and slope for mean sequential (SEQ) amplitude as a function of stimulus condition and allowing for random participant intercept and slope per stimulus condition. *Black bar:* Alternative LMM 1, using a fixed intercept and slope for mean sequential (SEQ) amplitude and allowing one random slope per participant. *White bar:* Alternative LMM 2, using a fixed intercept and slope for mean sequential (SEQ) amplitude as a function of stimulus condition and allowing one random slope per participant. *Yellow bar:* Alternative LMM 3, using a fixed intercept and slope for mean sequential (SEQ) amplitude as a function of stimulus condition and allowing a random slope per participant, per condition.

Supplementary Table 1.
Summary of suppression slopes for 9 visual areas and 4 stimulus conditions. *Data are scale factors and have arbitrary units. Data are from 10 participants, except for IPS0/1 (4 participants) and TO1/2 (8 participants). M: mean. SE: standard error.*

	Stimulus condition							
	Small & Short		Small & Long		Big & Short		Big & Long	
Visual area	*M*	*SE*	*M*	*SE*	*M*	*SE*	*M*	*SE*
V1	.85	.057	.81	.023	.84	.070	.85	.036
V2	.75	.028	.63	.023	.78	.037	.78	.055
V3	.67	.040	.59	.054	.74	.039	.70	.076
hV4	.64	.037	.40	.029	.66	.040	.62	.080
VO1/2	.65	.051	.40	.034	.70	.042	.62	.070
V3A/B	.66	.051	.39	.043	.67	.035	.65	.059
IPS0/1	.63	.061	.41	.054	.67	.10	.56	.056
LO1/2	.56	.057	0.27	0.041	.61	.051	.59	.064
TO1/2	.43	.057	0.24	0.043	0.47	0.019	.47	.11

Supplementary Table 2.

Post-hoc comparisons of suppression slopes, for each visual area and stimulus condition. Mean condition difference (C1 – C2), standard error (SE) and 95%-confidence intervals are have arbitray units (slope). P-values are Bonferroni corrected for multiple comparisons. *** $p < 0.001$, ** $p < 0.01$, * $p < 0.05$.

Visual area	Condition 1	Condition 2	C1 – C2	SE	$CI_{95\%}$ Lower	$CI_{95\%}$ Upper
V1	Short & big	Long & big	-.013	.076	-.21	.19
	Short & big	Short & small	-.0071	.076	-.21	.19
	Short & big	Long & small	.030	.076	-.17	.23
	Long & big	Short & small	.0054	.076	-.20	.22
	Long & big	Long & small	.042	.076	-.19	.24
	Short & small	Long & small	.037	.076	-.16	.24
V2	Short & big	Long & big	.047	.076	-.15	.25
	Short & big	Short & small	.032	.076	-.17	.23
	Short & big	Long & small	.15	.076	-.049	.35
	Long & big	Short & small	-.016	.076	-.22	.18
	Long & big	Long & small	.12	.076	-.096	.31
	Short & small	Long & small	.12	.076	-.080	.32
V3	Short & big	Long & big	.034	.076	-.17	.23
	Short & big	Short & small	.051	.076	-.15	.25
	Short & big	Long & small	.14	.076	-.057	.34
	Long & big	Short & small	.017	.076	-.18	.22
	Long & big	Long & small	.11	.076	-.091	.31
	Short & small	Long & small	.093	.076	-.11	.29
hV4	Short & big	Long & big	.043	.076	-.16	.24
	Short & big	Short & small	.025	.076	-.18	.23
	Short & big	Long & small	.27**	.076	.066	.47
	Long & big	Short & small	-.018	.076	-.22	.18
	Long & big	Long & small	.22*	.076	.022	.42
	Short & small	Long & small	.24**	.076	.040	.44
VO1/2	Short & big	Long & big	.086	.076	-.11	.29
	Short & big	Short & small	.056	.076	-.14	.26
	Short & big	Long & small	.30***	.076	.10	.50
	Long & big	Short & small	-.030	.076	-.23	.17
	Long & big	Long & small	.22*	.076	.016	.42
	Short & small	Long & small	.25**	.076	.046	.45
V3A/B	Short & big	Long & big	.033	.076	-.17	.23
	Short & big	Short & small	.027	.076	-.17	.23
	Short & big	Long & small	.30***	.076	.099	.50
	Long & big	Short & small	-.0061	.076	-.21	.19
	Long & big	Long & small	.27**	.076	.066	.47
	Short & small	Long & small	.27**	.076	.072	.47
IPS0/1	Short & big	Long & big	.12	.12	-.21	.42
	Short & big	Short & small	.042	.12	-.27	.36
	Short & big	Long & small	.26	.12	-.056	.58
	Long & big	Short & small	-.064	.12	-.38	.25
	Long & big	Long & small	.16	.12	-.16	.47
	Short & small	Long & small	.22	.12	-.098	.54
LO1/2	Short & big	Long & big	.027	.076	-.17	.23
	Short & big	Short & small	.058	.076	-.14	.26
	Short & big	Long & small	.35***	.076	.15	.55
	Long & big	Short & small	.030	.076	-.17	.23
	Long & big	Long & small	.32***	.076	.12	.52
	Short & small	Long & small	.29***	.076	.091	.49
TO1/2	Short & big	Long & big	.14	.084	-.086	.36
	Short & big	Short & small	.040	.084	-.18	.26
	Short & big	Long & small	.24*	.084	.013	.46
	Long & big	Short & small	-.098	.084	-.32	.13
	Long & big	Long & small	.10	.084	-.12	.32
	Short & small	Long & small	.20	.084	-.027	0.42

Supplementary Table 3.

Post-hoc comparisons of pRF model performance. Mean model difference (M1 – M2), standard error and 95%-confidence intervals are in units of percent cross-validated variance explained. P-values are Bonferroni corrected for multiple comparisons. *** $p < 0.001$, ** $p < 0.01$, * $p < 0.05$.

Visual area	Model 1	Model 2	M1 – M2	SE	$CI_{95\%}$ Lower	$CI_{95\%}$ Upper
V1	CSS	LSS	-1.38***	0.24	-1.95	-0.804
	CST	CSS	6.54***	0.24	5.97	7.12
	CST	LSS	5.17***	0.24	4.59	5.74
V2	CSS	LSS	-0.41	0.24	-0.98	0.164
	CST	CSS	9.33***	0.24	8.76	9.90
	CST	LSS	8.92***	0.24	8.35	9.49
V3	CSS	LSS	0.25	0.24	-0.32	0.819
	CST	CSS	10.42***	0.24	9.85	11.0
	CST	LSS	10.67***	0.24	10.10	11.2
hV4	CSS	LSS	3.21***	0.32	2.45	3.97
	CST	CSS	8.02***	0.32	7.26	8.77
	CST	LSS	11.23***	0.32	10.47	12.0
VO1/2	CSS	LSS	4.92***	0.38	4.02	5.82
	CST	CSS	8.88***	0.38	7.98	9.78
	CST	LSS	13.80***	0.38	12.90	14.7
V3A/B	CSS	LSS	1.02***	0.26	0.39	1.65
	CST	CSS	8.63***	0.26	8.00	9.26
	CST	LSS	9.65***	0.26	9.02	10.3
IPS0/1	CSS	LSS	2.77**	0.78	0.91	4.63
	CST	CSS	6.77***	0.78	4.91	8.62
	CST	LSS	9.53***	0.78	7.68	11.4
LO1/2	CSS	LSS	1.16***	0.23	0.61	1.71
	CST	CSS	4.44***	0.23	3.89	5.00
	CST	LSS	5.60***	0.23	5.05	6.15
TO1/2	CSS	LSS	3.95***	0.56	2.60	5.30
	CST	CSS	3.34***	0.56	1.99	4.69
	CST	LSS	7.29***	0.56	5.95	8.64